215 GHz for monitoring ice clouds: Comparison with radar/lidar synergy

2.2.1 Introduction

The proposals for cloud-profiling satellites by ESA and NASA have both considered a payload of a 94 GHz radar and a visible lidar; the very different scattering behaviour of the two instruments would enable aerosols, rain, and cloud of all types to be detected. In section 2.5 we will show how lidar and radar can be used to infer the presence of supercooled water layers embedded within ice clouds, but the main intended synergetic use of the two instruments is in the retrieval of the microphysical characteristics of purely ice clouds; because the radar return is approximately proportional to the sixth power of diameter while the lidar echo is proportional to the second, the radar/lidar backscatter ratio is a potentially very sensitive measure of crystal size. Preliminary demonstrations of the retrieval of ice cloud parameters by this method have been presented by Intrieri et al. (1993), Donovan et al. (1999) and Donovan and van Lammeren (2000). The main problem to overcome is attenuation of the lidar signal, which can be substantial and is difficult to correct for given the uncertainty in the extinction-to-backscatter ratio. From space the occurrence of multiple scattering can also significantly degrade the retrievals. The penetration depths of a spaceborne lidar signal are estimated in section 2.3. In this section we take a different approach and examine the potential of dual-wavelength radar for the quantitative determination of ice crystal size and ice water content (IWC). In particular the combination of 94 GHz and 215 GHz is considered.

The use of dual-wavelength radar for measuring mean crystal size in cirrus was first proposed by Matrosov (1993); the longer wavelength radar scatters in the Rayleigh regime while the shorter wavelength radar scatters in the Mie regime such that the dual-wavelength ratio (DWR), defined simply as

$$\mathrm{DWR} = 10 \log_{10} \left(\frac{Z_\mathrm{l}}{Z_\mathrm{s}} \right) \quad \mathrm{dB} \tag{2.1}$$

(where Z_l and Z_s are the radar reflectivity factors, in $\mathrm{mm}^6\mathrm{m}^{-3}$, at the longer and shorter wavelengths respectively), is directly related to size. The estimate of size then enables IWC to be estimated more accurately than would be possible with a single radar. The technique has been demonstrated using observations at 35 GHz and 94 GHz by both Sekelsky et al. (1999) and Hogan et al. (2000a). However, for the typical range of crystal sizes found in cirrus, DWR tends to be less than 4 dB at these frequencies, and for crystals with diameters smaller than around 150 μm is generally to small to be measurable. This problem could be solved by using higher frequencies, for which DWR would be higher for a given crystal size, but for observing cirrus from the ground such instruments tend not to be feasible because the higher frequencies suffer much stronger attenuation by both boundary-layer water vapour and low-level liquid water clouds. Figure 2.1 shows the variation of attenuation coefficient with frequency in dry and humid atmospheres. The only meteorological radar constructed with a frequency above 95 GHz that the authors are aware of is the 215 GHz described by Mead et al. (1989). They presented observations of low-level fog, but attenuation was found to be too great to make quantitative measurements in ice clouds.

From space, however, the problem of penetrating the strongly-attenuating moist boundary layer disap-

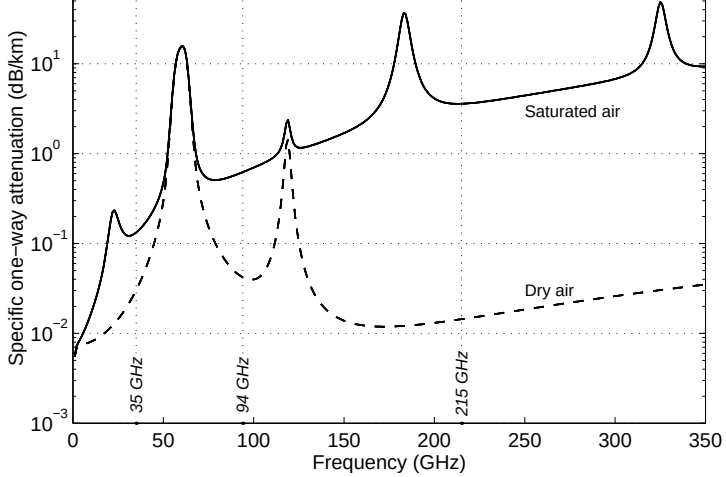

Figure 2.1: One-way attenuation due to atmospheric gases as a function of frequency, for dry and saturated air at 1000 mb and 10°C. The values were calculated using the line-by-line model of Liebe (1985). The three frequencies considered in this section lie in the minima between the various absorption bands and are shown by the vertical dotted lines.

pears, and frequencies as high as 215 GHz become a realistic possibility. The advantages of using higher frequencies in ice cloud are as follows:

1. A large increase in DWR for a given mean crystal size, enabling more a accurate size retrieval and the ability to measure down to smaller sizes.
2. Higher sensitivity: in the Rayleigh regime, reflectivity increases as the fourth power of frequency for a fixed antenna size, although this is partially countered by increased thermal noise and reduced power output. Mead et al. (1989) achieved a net increase in sensitivity of 2.2 dB with a transmitting tube very similar to those used in 94 GHz systems; the reduction in output power by 12.2 dB was more than offset by the 14.4 dB increase in sensitivity due to increased scattering efficiency.
3. A smaller beamwidth and footprint for a given antenna size, resulting in a better match with a spaceborne lidar. The 94 GHz radar considered for the Earth Radiation Mission (ERM) would have an antenna with a diameter of around 2 m, resulting in a footprint of 700 m (-3 dB, one-way). The same antenna at 215 GHz would result in a footprint of around 305 m.
4. A closer correlation between IWC and Z for a single higher frequency radar. This is because the effect of Mie scattering is to reduce the power dependence of Z on diameter from 6 to something closer to that of IWC.

In this section we study the case for a 215 GHz spaceborne radar, both in single- and dual-wavelength scenarios. Extensive use is made of ice crystal size spectra collected by the UK Met Office C-130 aircraft during the European Cloud Radiation Experiment (EUCREX). In previous papers (Brown et al. 1995, Hogan and Illingworth 1999b), use was also made of aircraft-measured ice crystal spectra from the Central Equatorial Pacific Experiment (CEPEX), but unfortunately these data are not available classified

is quantified, and then the magnitude of the attenuation to be expected when penetrating a number of 'standard' atmospheres is calculated. In section 2.4 we estimate the magnitude of the error introduced by mounting the two instruments of a dual-wavelength system (both radar/radar and radar/lidar) on separate satellite platforms.

2.2.2 Calculating reflectivity from aircraft size spectra

We first determine the effect of using a very high frequency radar on the relationship between radar reflectivity (Z) and ice water content (IWC), by calculating these parameters from more than 11 000 mid-latitude ice cloud size spectra observed in EUCREX. Each of the spectra was a 5-s average, and the total dataset corresponded to over 15 hours of flight through around 7 000 km of cloud. The size spectra were compiled from 2D imaging probes mounted on the C-130 that observed particles in the diameter range 25–6400 μm. Previous analysis of such data in terms of radar reflectivities (Atlas et al. 1995, Brown et al. 1995, Hogan and Illingworth 1999b) involved approximating the observed irregular particles to homogeneous ice-air spheres, in order that Mie theory could be applied. Typically the diameter of the sphere was calculated from the observed maximum dimensions of the image, such that it represented an 'envelope' that encompassed the entire crystal. In order that the IWC calculated from the size spectra agrees with those from other bulk water measurements on the aircraft, it was found by Brown and Francis (1995) that one must assume the crystals to be composed of a mixture of ice and air with a density that decreases with increasing diameter. However, it is far from clear that the resulting *reflectivities* are accurate, particularly at 215 GHz where Mie scattering is very significant; by using a homogeneous sphere that fully envelops the observed crystal one is essentially moving ice mass from the centre (where one would expect it to be concentrated in a real crystal) to the periphery, and thereby increasing the extent of Mie scattering.

In this study we attempt to lessen this problem by classifying the observed crystal images by area rather than maximum dimension; the 'equivalent area' diameter (D_a) is invariably less than the 'envelope' diameter (D_m) , and the scattering properties of a sphere with a diameter D_a should hopefully be closer to those of the real crystal. Francis et al. (1998) compared IWC from area-binned size spectra with bulk measurements, and from their results we derive the following expression for effective crystal density (ρ):

$$\rho = 0.175 D_\mathrm{a}^{-0.66} \ \ \mathrm{gm}^{-3}. \tag{2.2}$$

Radar reflectivity at frequency f is then given by

$$Z_f = \int_0^\infty \frac{|K(\rho)|^2}{0.93} n(D_\mathrm{a}) D_\mathrm{a}^6 \gamma_f(D_\mathrm{a})\, dD_\mathrm{a}, \tag{2.3}$$

where $n(D_\mathrm{a})$ is the number concentration in the size range $D_\mathrm{a} \rightarrow D_\mathrm{a} + dD_\mathrm{a}$, γ_f is the Mie-to-Rayleigh ratio, and K is given by

$$K = \frac{\varepsilon - 1}{\varepsilon + 2}. \tag{2.4}$$

The complex dielectric constant of the ice-air mixture, ε, is calculated using the formulae of Liebe et al. (1989) and Meneghini and Liao (1996). The factor 0.93 is present to ensure that Z is relative to liquid water at centimetre wavelengths, and hence to enable comparison of different wavelengths.

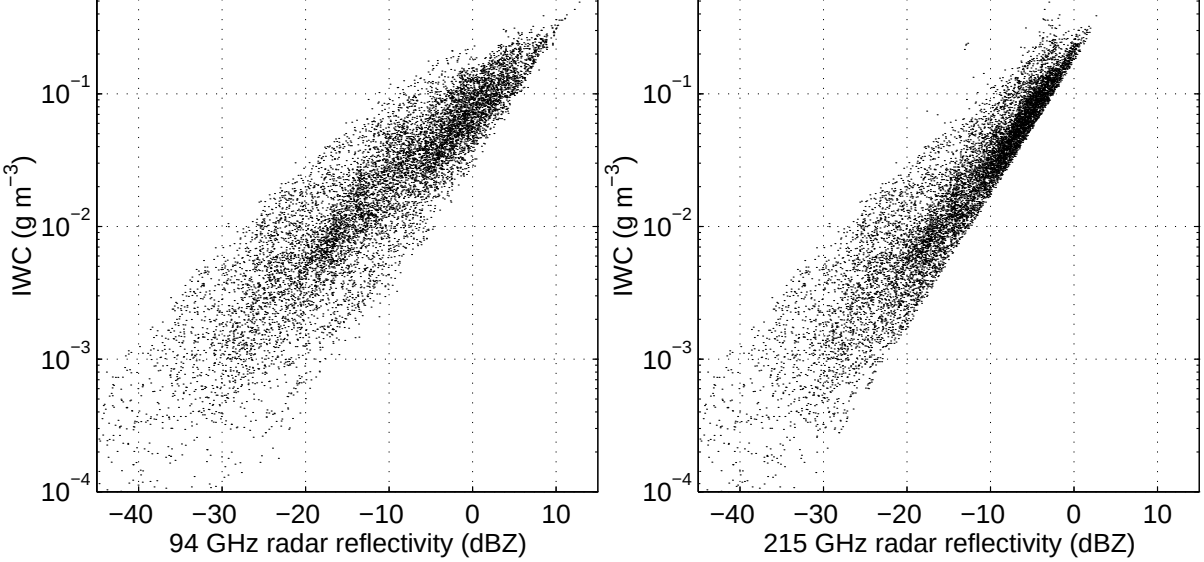

Figure 2.2: Scatterplots of IWC versus 94 GHz and 215 GHz radar reflectivity for the EUCREX aircraft spectra. Over 11 000 observations are present, representing around 15 hours of data in mid-latitude ice cloud.

Validation of radar reflectivity calculated from aircraft size spectra have so far been rather limited. At Rayleigh-scattering frequencies we are confident that Z calculated from aircraft microphysical measurements is fairly accurate, since the reflectivity of a single crystal is proportional to the square of its mass, but insensitive to size of particle over which the mass is distributed. This was confirmed during the ESA Cloud Lidar and Radar Experiment (CLARE'98) by simultaneous measurements with the C-130 aircraft and the scanning 3 GHz radar at Chilbolton, England (see Hogan and Goddard 1999 for an example). At 94 GHz, validation is more troublesome because attenuation (predominantly by water vapour) greatly reduces the range out to which comparison can be performed. Donovan et al. (1999) found reasonable agreement between the Z in ice cloud measured by an airborne 95 GHz radar with the values calculated from in situ measurements (using both area- and D_{m}-binned spectra), although there were some uncertainties regarding the calibration of that particular radar. Hogan et al. (2000a) showed from scattering calculations that the assumed density could affect IWC and particle size retrievals using dual-wavelength radar at 35 GHz and 94 GHz by as much as a factor of two. This would be no less true at 215 GHz, and for radar/lidar retrievals, so there is clearly both more theoretical and observational work to be done.

2.2.3 Relationship between radar reflectivity and IWC

It was shown by Brown et al. (1995) that the reflectivity from a single 94 GHz radar can be used to estimate IWC with an rms error of around a factor of two. Figure 2.2 shows scatterplots of IWC against Z at both 94 GHz and 215 GHz calculated from the area-binned EUCREX spectra. The beneficial effect of Mie scattering at 215 GHz to reduce the strong dependence of Z on size noticeably reduces the scatter, particularly for the most radiatively significant clouds with the highest values of IWC: above 0.1 g m^{-3} the rms error at 215 GHz falls to $+50\%$ and -35% (around a factor of 1.5). Interestingly, this is the

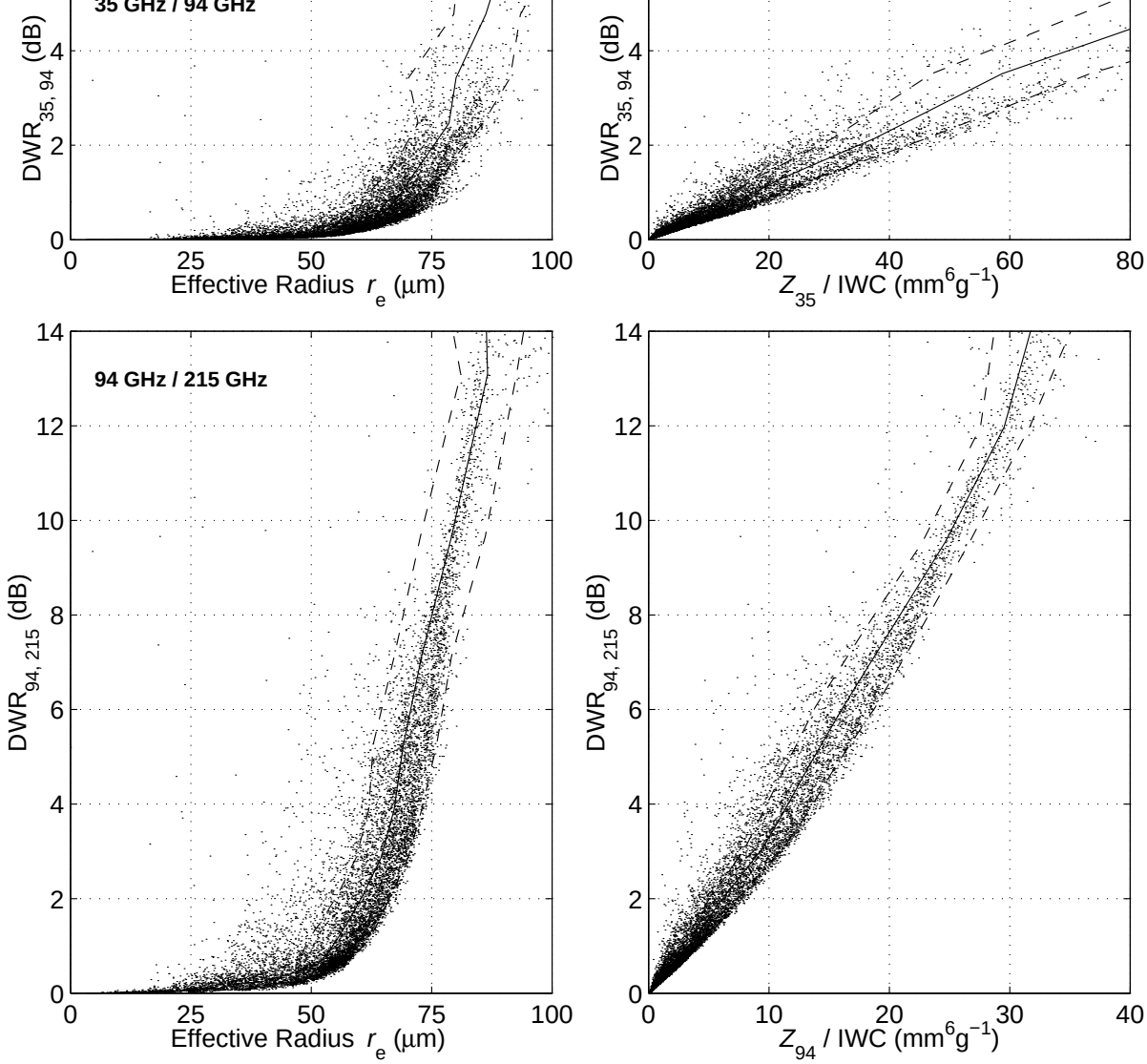

Figure 2.3: Scatterplots of dual-wavelength ratio (DWR) versus effective radius and the ratio of reflectivity to ice water content. The top panels are for a dual-wavelength combination of 35 GHz and 94 GHz, and the bottom panels correspond to the 94 and 215 GHz combination. The solid lines depict 'best-fit' relationships between the various parameters and the dashed lines correspond to one standard deviation from the mean. These data were calculated from the area-binned EUCREX size spectra in mid-latitude ice cloud.

same value as the accuracy that Brown et al. (1995) calculated for IWC retrievals using a 94 GHz radar when some measure of size was available in addition to the radar reflectivity. It should be noted that if frequencies lower than 94 GHz are used then the scatter becomes appreciably worse.

To fully constrain the radiation budget it is necessary to obtain some measure of ice crystal size, in addition to IWC. The most commonly-used size parameter in clouds is effective radius (r_e), which following Francis et al. (1994) we define as

$$r_e = \frac{3}{4}\frac{\mathrm{IWC}}{\rho_i \int_0^\infty n(A) A \, dA}, \tag{2.5}$$

where ρ_i is the density of solid ice and A is the ice crystal cross sectional area. When area-binned data are used, A can of course be calculated exactly. Effective radius should be directly related to DWR. Additionally, we can relate DWR to the ratio between reflectivity at the longer of the two wavelengths and IWC; in this way the combination of Z and DWR allows IWC to be measured more accurately than is possible from Z alone.

Figure 2.3 shows scatterplots of DWR versus both r_e and the ratio of Z to IWC, calculated from the EUCREX data binned by area. We have used both the 35/94 GHz and 94/215 GHz frequency combinations, and it can be seen instantly that the sensitivity of DWR to size effects is much stronger when the higher of the two frequencies is 215 GHz. For the 35/94 GHz combination, DWR tends not to exceed 4 dB (consistent with the observations of Hogan et al. 2000a), whereas for the 94/215 GHz combination it can attain values of 10 dB. Also shown are lines of best fit, calculated by interpolating between the mean values of r_e and Z/IWC in unequally-spaced ranges of DWR. The dashed lines are one standard deviation from the mean, and indicate that both IWC and r_e could be retrieved with an rms error of as little as 10–20%. These values are in broad agreement with those of Hogan and Illingworth (1999b), but their lines of best fit were different by up to a factor of two because they used aircraft size spectra binned by D_m. It only after the issue of interpretation of aircraft data in terms of radar reflectivity is resolved that retrieval errors as low as 20% could be realised.

Dual-wavelength radar has the potential to make very useful measurements when the particles are sufficiently large that DWR is greater than around 1 dB, but the limitation is clearly for the small crystals that have a DWR only slightly greater than 0 dB. This is of particular significance for a spaceborne radar which must use short dwells (around 1 s) to maintain horizontal resolution, thus limiting the precision of Z compared to ground-based systems which can integrate over several minutes if necessary. In the processing of cloud radar data, the contribution to the signal from thermal and instrumental noise is usually subtracted. This enables the radar to detect genuine meteorological signals that are 15 dB smaller than the noise signal, although the accuracy of the measurements at low signal-to-noise ratios is much worse. It can be shown (e.g. Hogan 1998) that for a radar with a noise-equivalent reflectivity for a single pulse N (in dBZ), the standard error of a reflectivity measurement averaged over M independent pulses is given approximately by

$$\Delta Z \simeq \frac{4.343}{\sqrt{M}}\left[1 + 10^{0.1(N-Z)}\right] \quad \mathrm{dB}. \tag{2.6}$$

It is valid to assume that all pulses of a spaceborne radar are independent, so for the radar proposed for the ERM with a pulse repetition frequency of 5500 Hz, a 1.4-s dwell (10 km along-track averaging) corresponds to $M = 7700$. ESA (1999) defined a cloud to be detectable if it had a 'radiometric resolution' of less than 1.44 dB, equivalent to setting the maximum-allowable ΔZ to 1.7 dB. Figure 2.4 shows ΔZ versus Z for a a radar with a 'minimum detectable reflectivity' (in the absence of attenuation) of -36.8 dBZ. This was the value calculated by ESA (1999), although their definition of Z resulted in a value 1.3

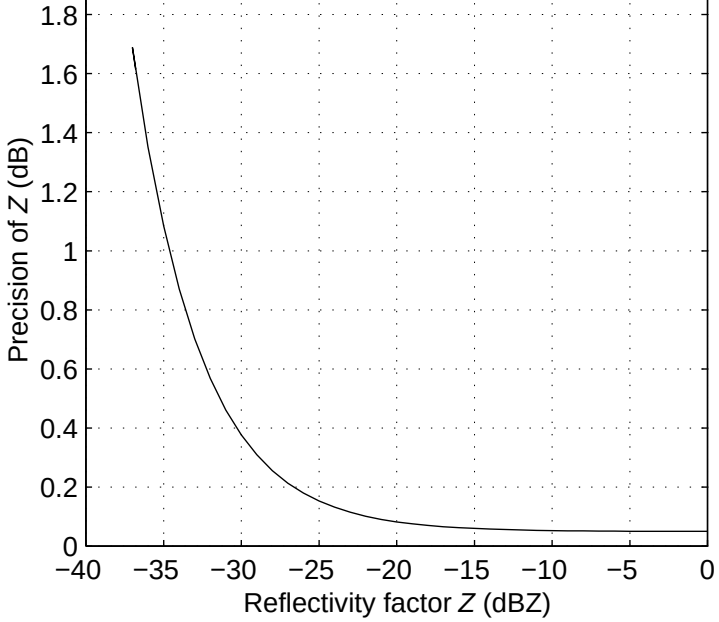

Figure 2.4: The precision of measured radar reflectivity for 7700-pulse averaging (10 km) and a noise-equivalent reflectivity of -22.2 dBZ.

dB higher. The error in DWR is given by

$$\Delta\mathrm{DWR} = \left(\Delta Z_{\mathrm{l}}^2 + \Delta Z_{\mathrm{s}}^2\right)^{1/2} \quad \mathrm{dB}. \tag{2.7}$$

At large signal-to-noise ratios $\Delta Z \rightarrow 0.05$ dB, and so assuming the two radars are equally sensitive, $\Delta\mathrm{DWR} \rightarrow 0.07$ dB. For the 35/94 GHz dual-wavelength combination this corresponds to a minimum-measurable r_{e} of around $45\,\mu$m, while for the 94/215 GHz combination this puts a lower limit to the measurable r_{e} of around $25\,\mu$m. However, in many situations where small particles are present, the reflectivity will be low, and the corresponding error in DWR could be too high for accurate size retrieval. Figure 2.5 shows the fraction of clouds for which size can be estimated as a function of Z for the two wavelength combinations 35/94 GHz and 94/215 GHz. In each case, two criteria for acceptable errors in DWR have been considered; the solid line corresponds to $\mathrm{DWR} > \Delta\mathrm{DWR}$ and the dashed line is for $\mathrm{DWR} > 2\Delta\mathrm{DWR}$. As expected the fraction of clouds that can be sized increases rapidly as the signal-to-noise ratio increases. Considering the second and more stringent of the two criteria, we see that only around 20% of clouds with a reflectivity of -20 dBZ could be sized by a 35 GHz and 94 GHz dual-wavelength radar, but this value rises to around 85% for the 94 GHz and 215 GHz combination.

2.2.5 Attenuation at 215 GHz

We have demonstrated several advantages in using 215 GHz radar to observe ice clouds from space. The only disadvantage when compared to 94 GHz would appear to be the higher attenuation, which we shall quantify now. The nadir two-way gaseous attenuation from space has been calculated using the line-by-line model of Liebe (1985), for three standard atmospheres taken from McClatchey et al. (1972),

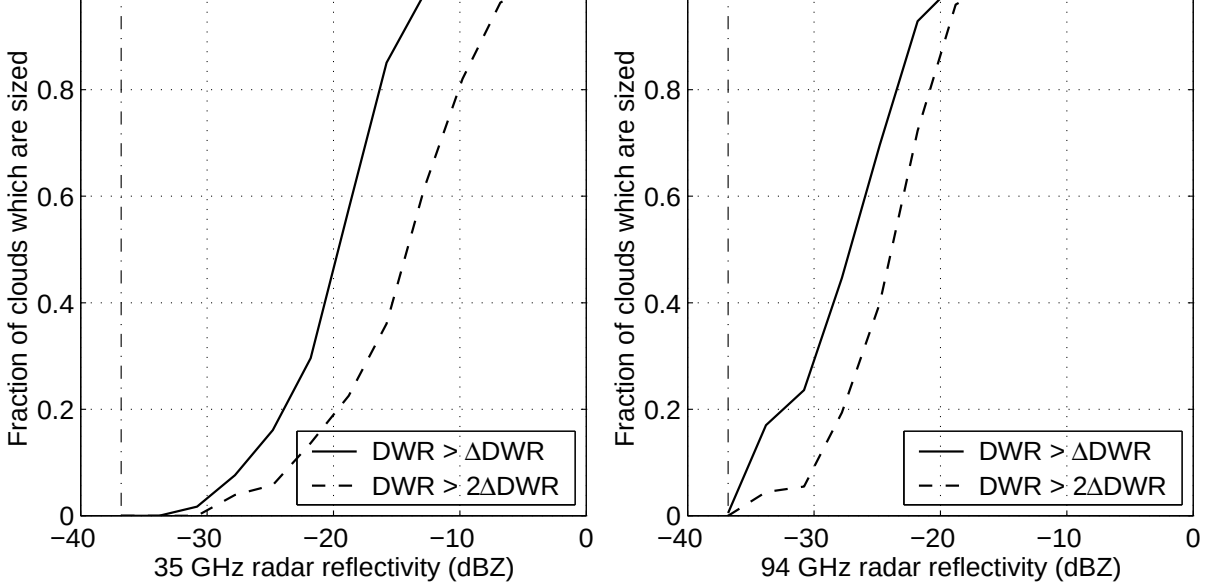

Figure 2.5: The fraction of detected cloud that can be sized by a dual-wavelength radar with a minimum-detectable reflectivity of -36.8 dBZ (shown by the vertical dot-dashed line). The two panels correspond to the two wavelength combinations under consideration.

but with saturated layers added at altitudes typical of cirrus. Figure 2.6 shows the profiles of temperature, relative humidity and the corresponding two-way nadir attenuation at five different frequencies. In mid-latitude summer and the tropics it can be seen that the attenuation at 0°C (4 km) reaches at most around 0.4 dB at 94 GHz and 2 dB at 215 GHz. This is not a great problem for a 94/215 GHz dual-wavelength system since the reflectivity at 215 GHz can be matched with the 94 GHz value in the Rayleigh-scattering cloud top, and the attenuation then corrected through the remainder of the cloud assuming the relative humidity to be 100% wherever there is a cloud echo. In any case, the crystals at the base of a thick cloud are likely to be large enough that even an error in DWR of 1 dB after attenuation correction is likely to be significantly less than the magnitude of DWR due to Mie scattering, and the retrieved size should not be greatly biased.

The attenuation by the ice crystals themselves also increases with frequency, but is still a much smaller effect than attenuation by water vapour. At 94 GHz it can be neglected, and at 215 GHz it has been calculated from aircraft datasets by that only 2.1% of tropical cirrus and 0.2% of mid-latitude cirrus should have a two-way extinction of greater than 1 dB km^{-1} (Hogan and Illingworth 1999b).

Clearly 215 GHz is not a good choice of wavelength if detection of low stratocumulus is a priority; the two-way attenuation to the ground is around 20 dB in the case of mid-latitude summer and tropical cases. In any case, it is doubtful that the radar return from stratus and stratocumulus can be used quantitatively since the ubiquitous presence of the occasional drizzle drop means that Z is essentially unrelated to liquid water content (Fox and Illingworth 1997).

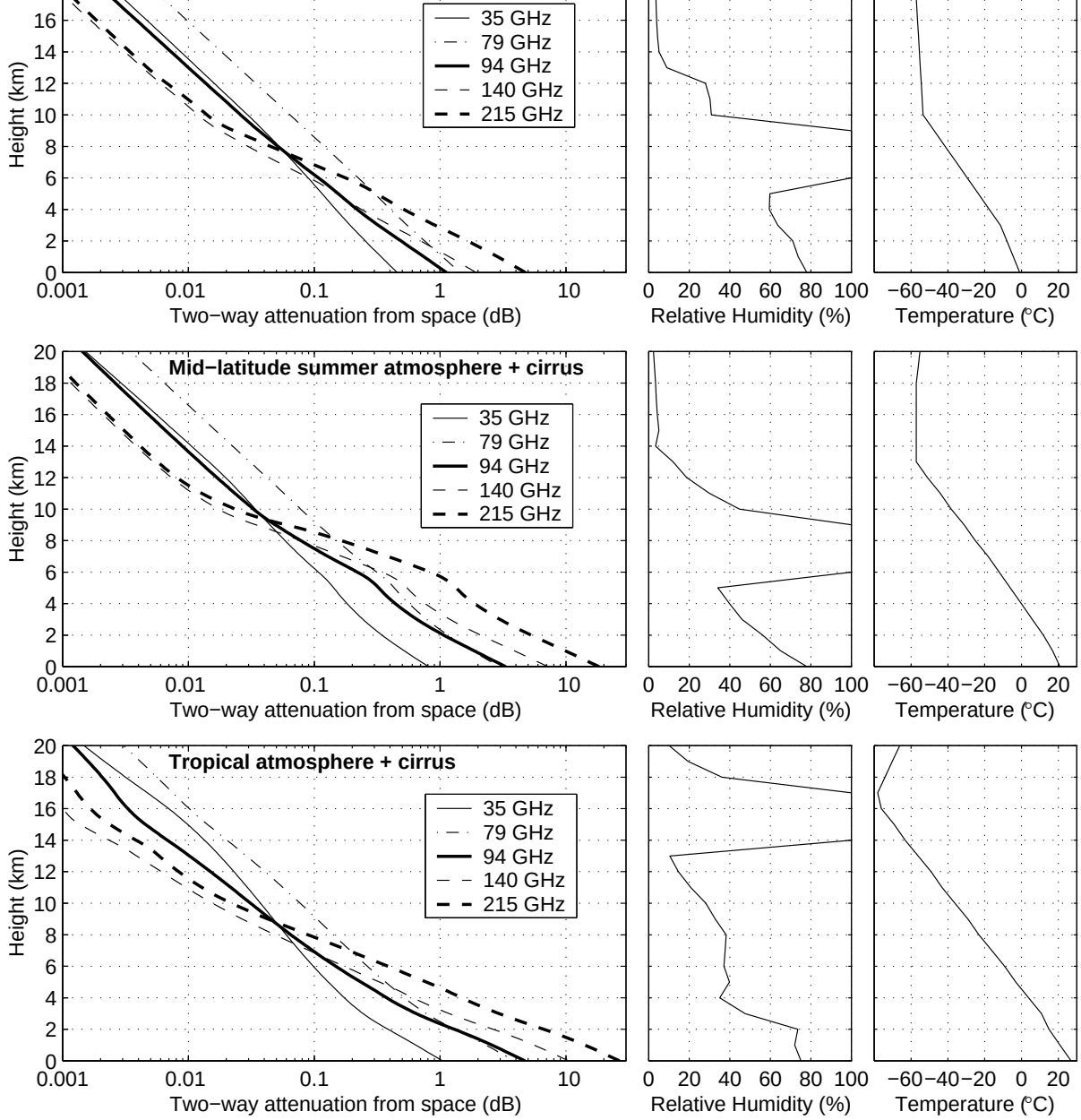

Figure 2.6: The two-way attenuation from space at five frequencies for three standard atmospheres with cirrus added at typical altitudes.

2.2.6 Conclusions

We have explored the feasibility of spaceborne 215 GHz radar in both single- and dual-frequency configurations. For a single frequency system, 215 GHz has several advantages over the more usually considered frequency of 94 GHz, the principle one of which is that IWC can be more accurately estimated from Z alone. At 215 GHz the error in IWC decreases from $+140\%/-60\%$ for IWC ~ 0.001 g m^{-3} to $+50\%/-35\%$ for IWC ~ 0.1 g m^{-3}, while at 94 GHz it is somewhat higher, falling from $+200\%/-65\%$ for IWC ~ 0.001 g m^{-3} to $+65\%/-40\%$ for IWC ~ 0.1 g m^{-3}. Additionally, the higher frequency

attenuation at 215 GHz in ice clouds is generally small enough not to detrimentally affect the retrievals. However, if the detection of low clouds is a priority then 215 GHz is not a suitable choice for a single-wavelength system since the two-way attenuation can be as much as 20 dB in the lowest 3 km. In the next section we attempt to quantify the lidar attenuation in real ice clouds for comparison with the 215 GHz values.

Our results suggest that dual-wavelength 94/215 GHz radar has the potential measure r_e and IWC to better than 20%. The technique is most effective in the thicker, more radiatively significant clouds where the crystals are large enough to Mie scatter significantly at 215 GHz. It is these clouds that would be most attenuating for the lidar, and therefore the most difficult to size using the radar/lidar method. It should be noted that the estimated accuracy of dual-wavelength radar retrievals is somewhat of a best guess; there is still much uncertainty as to how to represent the density of ice crystal in scattering calculations. However, this is no less true of the theoretical work underlying radar/lidar retrieval algorithms. Unfortunately the problem of boundary-layer attenuation makes it very difficult to use a real ground-based 215 GHz system to validate retrievals techniques in ice cloud, so if such an instrument were to be considered seriously for a satellite mission, data would need to be taken by an airborne 215 GHz radar.

It is interesting to compare the values of attenuation at 215 GHz with those for a spaceborne lidar. We have estimated the lidar attenuation from space using 2.5 months of data recorded by the vertically-pointing 94 GHz Galileo radar at Chilbolton, England, between 5 November 1998 and 24 January 1999. Radar reflectivity was converted to lidar extinction coefficient (α) using the following formula, which was derived as a best-fit to the EUCREX area-binned aircraft data:

$$\log_{10}(\alpha) = 0.546\, Z_{94} - 2.7131, \tag{2.8}$$

where α has the units m^{-1} and Z_{94} is in dBZ. The radar was carefully calibrated during the CLARE'98 campaign (Hogan and Goddard 1999), but it has been necessary to add a fixed value of 2 dB to the Z values to very roughly account for water vapour attenuation through the boundary layer. It should be noted that there is a considerable degree of scatter in the relationship between Z and α, and also that these observations take no account of the presence of highly-attenuating supercooled liquid water clouds (studied later in this report), so the estimates of lidar attenuation should be regarded as rather preliminary and if anything rather conservative. The results are shown in Fig. 2.7. The left panel shows the frequency that the attenuation down to any pixel in the atmosphere would exceed a particular value. At a height of 4 km, we see that around 25% of the pulses would be attenuated by more than 3 dB (two way), while 15% would be attenuated by 10 dB or more. However, this is misleading since we are obviously only interested in lidar returns when there is some cloud present. When only the attenuation down to cloudy pixels is considered (right panel) the results for the spaceborne lidar are considerably worse: 73% of the returns from cloud at 4 km would be attenuated by at least 3 dB, and 53% of them by at least 10 dB.

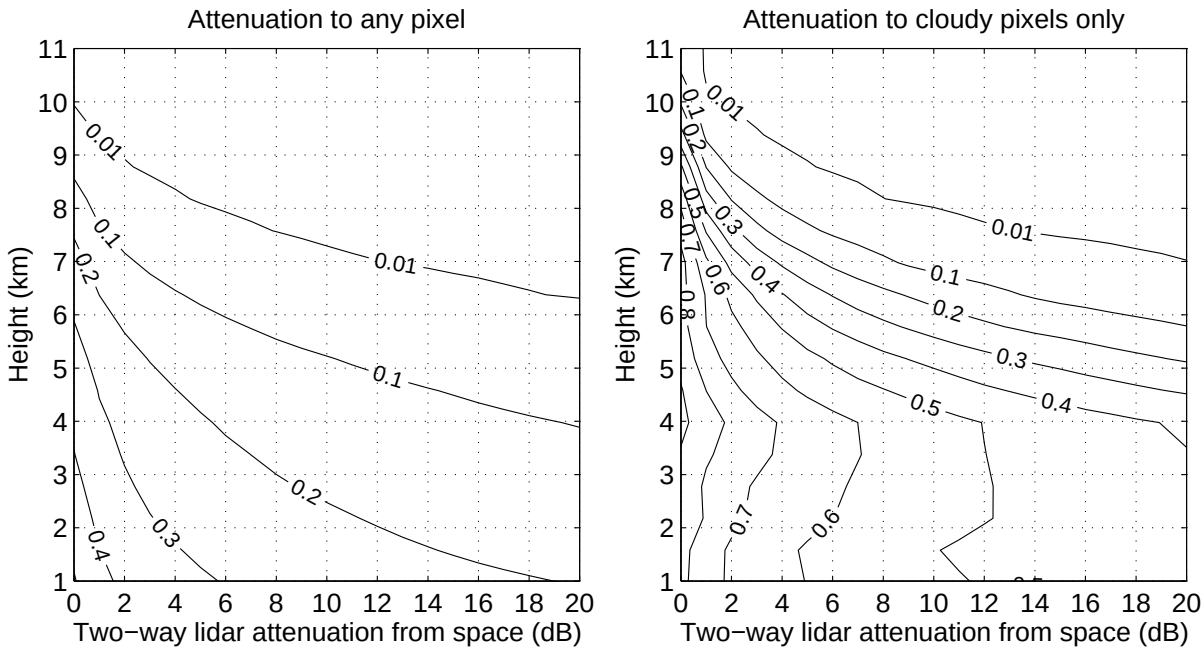

Figure 2.7: Frequency that the attenuation of the signal from a spaceborne lidar through ice cloud would exceed a given amount. The left plot considers the penetration down to any pixel, while the right plot considers only penetrations down to cloudy pixels. These values were estimated from 76 days of continuous 94 GHz radar observations at Chilbolton during winter 1998/1999.

at 215 GHz by water vapour and ice clouds appears rather small by comparison, and suggests that for many clouds dual-wavelength radar would be more effective for IWC and size retrievals than a radar and lidar.

2.4.1 Introduction

Financial constraints may exclude the possibility of a payload of two active instruments on a cloud profiling satellite, and the alternative currently proposed by NASA is to mount the radar and the lidar on two separate satellites in very close orbits. Since clouds can be very inhomogeneous it is important to determine how detrimental the separation of the footprints would be on the quality of the synergetic information, such as cirrus effective radius. ESA estimated that a second satellite could trail the first with the footprints drifting towards and away from each other by as much as 5 km. NASA on the other hand believe that the orbits and instrument pointing angles can be configured such that the lidar footprint would nearly always lie within the wider swath of the radar.

In this section synthetic cirrus cloud fields are generated with the same spectral characteristics as those observed by ground based radars. The spaceborne radar and lidar, and the 94/215 GHz dual-wavelength radar, are 'flown' across the cloud fields with varying footprint separation, and the changes in the measured backscatter ratio are calculated as a function of footprint separation. By comparison of these errors with the range of values that the backscatter ratio can take with varying effective radius, we can determine whether the errors due to footprint separation are manageable, or whether they are so great that the 'Split Mission' scenario is not a viable option.

2.4.2 Generation of synthetic cloud fields

In order to estimate the magnitude of the errors arising from non co-located footprints we need to know the typical spatial structure of real cirrus clouds. This information has been obtained using vertically-pointing ground-based 35 GHz and 94 GHz observations at Chilbolton, England. Ten second averages of reflectivity factor were recorded with a vertical resolution of 75 m. Vertical averaging was performed to reduce the vertical resolution to 525 m, close to the 500 m proposed for a spaceborne radar. A number of 1024-point time-series of reflectivity factor (in dBZ) in cirrus were selected, and the temporal scale converted to a spatial scale using a simple Taylor transformation and the mean wind speed over Chilbolton at that time and altitude as diagnosed by the UK Met Office Mesoscale Model. Only time-series in which all points registered cloud were considered. Information on the horizontal structure was then obtained by fitting power laws of the form

$$E = E_0 \, k^{\mu} \tag{2.9}$$

to the Fourier spectra of these data, where k is wavenumber, E is power spectral density, and E_0 and μ are the coefficients. The best fit lines were least-squares fits in log-log space after 7-point averaging of the spectra to reduce scatter. The parameter μ was found to vary between -1.8 and -2.4 in cirrus, which compares with the range -1 to -2 found by Danne et al. (1996). No significant difference was found between the spectra measured by the 35 GHz and 94 GHz radars. A spectrum typical of those analysed is shown in Fig. 2.8. It had the form $E = 2.03 \times 10^{-5} k^{-2.16}$ dBZ^2 m (where k is in m^{-1}), and we will use this from now on.

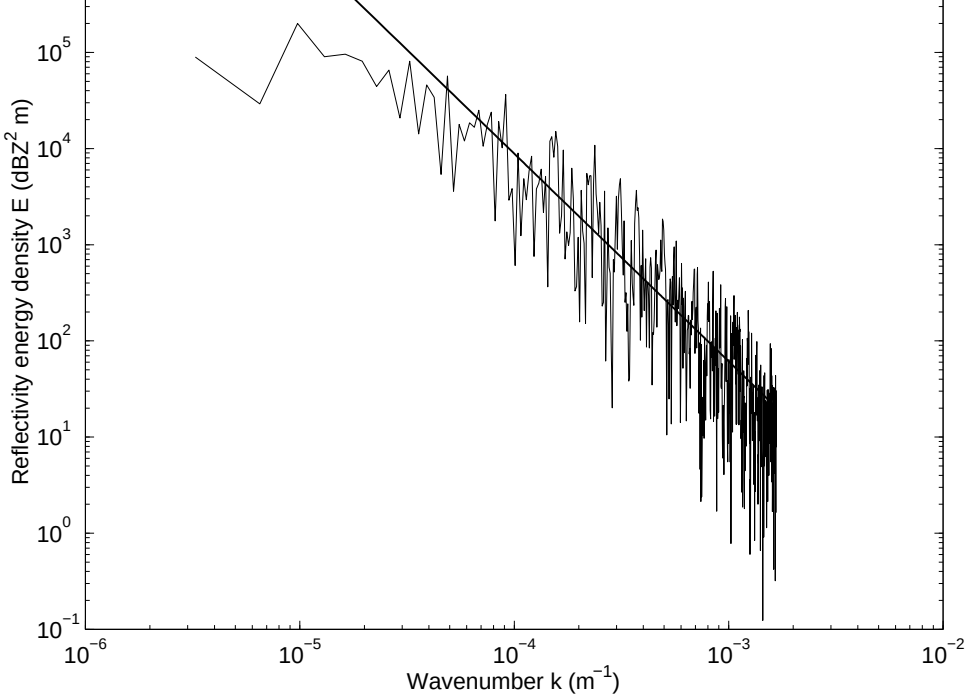

Figure 2.8: The power spectrum from 35 GHz reflectivity observations in cirrus at an altitude of 7 km. Time was converted to horizontal distance using a mean wind at this altitude of 30 m s^{-1}. The best fit line is $E = 2.03 \times 10^{-5} k^{-2.16}$.

Cloud fields were generated by calculating the inverse two-dimensional Fourier transform of synthetic matrices containing wave amplitudes consistent with the energy at the various scales indicated by the one-dimensional spectrum. See Hogan (1998) for a more complete explanation of the procedure. The phase of each wave component of the matrix was random, so that each cloud field was different. The domains were square and measured 25.6 km on a side with a resolution of 100 m. Fourier analysis of cross-sections through the domain confirmed that they had almost identical spectral properties as the original data. Note that the synthetic cloud fields are spectrally isotropic, whereas real cirrus clouds with fallstreaks are not because the fallstreaks tend to be aligned parallel to the vertical wind-shear vector. On average this is not expected to significantly bias the results.

2.4.3 Simulation of dual-wavelength radar overpasses

First the effect of separation on retrievals by dual-wavelength radar at 94 GHz and 215 GHz is determined, using 64 synthetic cloud fields generated using the procedure described above. The footprints of the 94 GHz and 215 GHz radar are taken to be 700 m and 305 m respectively, and Gaussian beam patterns are used. We consider swath lengths of 1 km and 10 km, corresponding to integration times of 0.14 s and 1.4 s respectively. It is assumed that we need only consider separations in the direction perpendicular to the direction of motion of the satellite; separations in the direction parallel to the motion of the satellites can in principle be corrected for by applying an appropriate time lag to the data from one of the instruments. This of course assumes that the cloud does not evolve significantly in the intervening

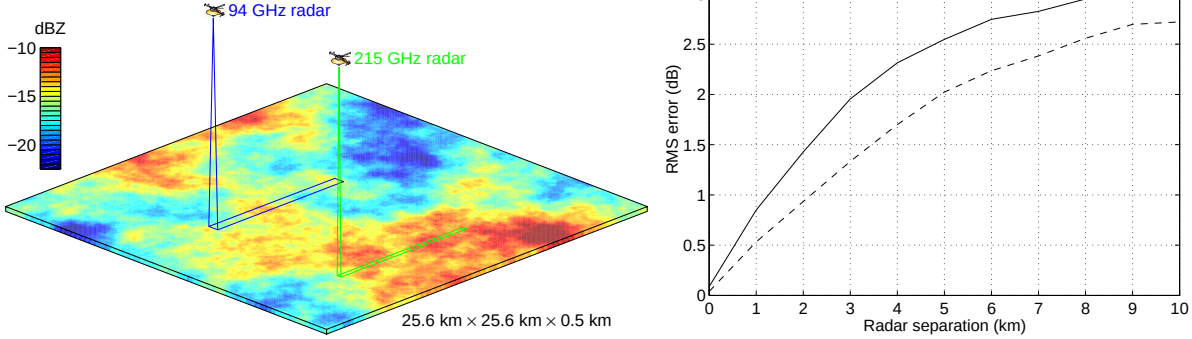

Figure 2.9: RMS error in the dual-wavelength radar ratio as a function of footprint separation.

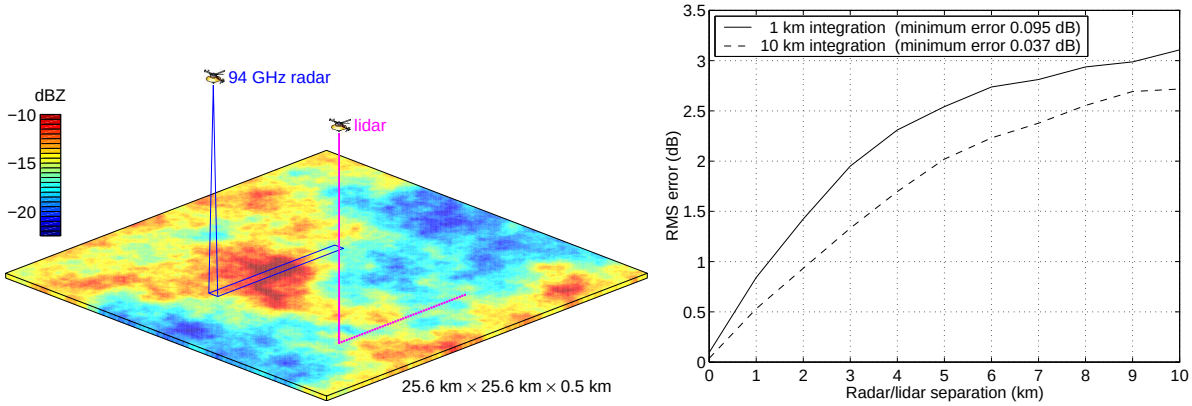

Figure 2.10: RMS error in the lidar/radar backscatter ratio as a function of footprint separation.

period.

The scenario for a 10 km integration is shown schematically in Fig. 2.9, along with the error in DWR as a function of separation, calculated from the results of flying the imaginary satellites over each of the 64 different cloud fields. We see that if the two radars were mounted on the same satellite such that their footprints were superposed, the error in DWR due to differences in footprint size would be less than 0.1 dB for both 1 km and 10 km integration. This is less than the random error due to a finite number of pulses being averaged, and is quite acceptable for crystal size retrieval. However, when the radars are separated by 5 km the error exceeds 2 dB, which from Fig. 2.3 we see would greatly degrade the size information available from the two instruments, and make sizing of the smaller crystals much more difficult. Hence for a dual-wavelength radar it would seem that there is little point in even attempting to derive size with errors of this magnitude.

2.4.4 Simulation of radar and lidar overpasses

The same synthetic cloud fields are now used to compute the effect of instrument separation on radar/lidar synergy. The lidar footprint is assumed to be 100 m across (1 pixel of the simulated cloud field), and we follow the specification of the ATLID instrument (ESA 1999) and assume a pulse repetition frequency of 35 Hz, which results in each footprint being 200 m apart. The radar reflectivity field is converted to

expressed logarithmically, the functional form of this relationship has *no effect* on the rms error of the backscatter ratio. This is shown in Fig. 2.10: the error in backscatter ratio (in dB) is almost exactly the same as for the dual-wavelength radar, except when the beams are entirely overlapped, for which the error is very slightly larger. This is simply because the difference in footprint size is greater. As before, a separation of 5 km results in an error of over 2 dB. Because the change in radar/lidar backscatter ratio with effective radius is much more than the change in dual-wavelength radar ratio, an error of 2 dB does not necessarily mean that particle sizing becomes impossible, although it is by no means insignificant.

2.4.5 Conclusions

We have examined the implications of the 'Split Mission' scenario on both radar/lidar and dual-wavelength radar retrievals using simulated but realistic 2D cloud fields. It is found that when the instruments are mounted on the same platform, the rms error is less than 0.1 dB, despite the differences in footprint size. If they are separated by 5 km then the error increases to more than 2 dB. This is unacceptable for a dual-wavelength radar. The radar/lidar technique is intrinsically more forgiving of errors (providing the lidar is corrected for attenuation) because the range over which the radar/lidar ratio varies with changing effective radius is so much greater, but certainly an error of this magnitude represents an unwelcome complication.

2.5.1 Introduction

Of primary importance in determining the radiative properties and evolution of a cloud is its phase. Mixed-phase clouds could potentially play an important role in the climate system (Sun and Shine 1995), but due to a lack of good observational datasets there is much uncertainty regarding the extent to which ice and liquid water coexist, and how to represent the ice to liquid water ratio below 0°C in forecast and climate models. Intuitively one might expect microscale coexistence of the two phases to be rare since such a situation is inherently unstable, with the ice crystals able to grow rapidly at the expense of the liquid water droplets by virtue of the difference in saturation vapour pressure (the 'Begeron-Findieson' mechanism). Most models crudely assume that the ice/liquid water ratio is a function of temperature alone, and varies smoothly from purely liquid water at 0°C to purely ice at some lower temperature. However, this lower temperature varies significantly among parameterisations (Smith 1990, Sundqvist 1993, Bower et al. 1996), and its value has been found to have a strong impact on mean cloud amount and consequently the radiation budget (Gregory and Morris 1996, Fowler and Randall 1996). From a large aircraft dataset, Moss and Johnson (1994) demonstrated that this lower temperature should be around −9°C, but there was considerable scatter in their data, clearly suggesting that temperature alone is not sufficient to characterise the ice/liquid water ratio. Indeed there is no reason to suppose that supercooled stratocumulus, altocumulus, cumulonimbus and fronts should each have the same relationship. More complex parameterisations have been proposed that make use of other model parameters such as vertical velocity (Tremblay et al. 1996, Wilson and Ballard 1999), but it is very likely that the formation of supercooled water (in stratiform rather than vigorously convective clouds) is subject to small-scale vertical motions that if averaged over a model gridbox would not be sufficient to cause condensation of liquid water. Furthermore, the rate of glaciation is very much dependent on how well the ice and liquid water are mixed within the gridbox.

There is clearly an urgent need for observations to improve our understanding of both the important microphysical processes that act in mixed-phase clouds and the resulting cloud-scale distribution of ice and liquid water. In situ aircraft measurements have been used to provide useful statistics on mixed-phase clouds, but to get an idea the overall cloud morphology requires high-resolution remote sensing techniques that have the ability distinguish liquid water from ice.

The most well-known method for remotely inferring cloud phase is the polarisation lidar technique; non-spherical ice crystals can be distinguished from liquid water droplets because they depolarise the incident light (Sassen et al. 1990). Eberhard (1995) proposed the use of dual-wavelength CO_2 lidar, which utilises the fact that the ratio of backscatter coefficient at suitably separated wavelengths is different for liquid droplets and ice crystals. The main limitation of ground-based lidars is that they are strongly attenuated by intervening liquid water clouds, so while they are useful for studying altocumulus (e.g. Sassen 1991, Heymsfield et al. 1991, Wylie et al. 1995), they cannot be used from the ground to study glaciating stratocumulus or the mixed-phase regions of precipitating frontal systems. Gosset and Sauvageot (1992) suggested using the differential attenuation of a dual-wavelength radar to retrieve liquid water content in a mixed-phase cloud, while the absolute value of radar reflectivity could be used to infer ice water content. However, if the wavelength of a radar is short enough for the attenuation through a cloud with

be unambiguously attributed to differential attenuation. Hogan et al. (1999) showed that ice crystals growing in the presence of supercooled water tend to be needles or plates with extreme aspect ratios, which can be detected by a polarisation radar as very high values of differential reflectivity. While this is useful for microphysical studies, it relies on ice being present, and cannot be used on its own to derive reliable statistics on the occurrence of supercooled water because it is such an indirect measurement.

In this section we demonstrate that supercooled water in the atmosphere often tends to occur in the form of layers composed of high concentrations of small droplets, which give a strong echo at the lidar wavelength, while the echo at the radar wavelength tends to be dominated by the contribution from the larger ice crystals so that the contribution from the supercooled layer is masked. This is demonstrated in Fig. 2.11, which shows a time-height section of lidar backscatter coefficient (β) from the 905 nm Vaisala CT75K lidar ceilometer at Chilbolton (resolution 30 m and 30 s) through a typical layer with a temperature of around $-20°$C. The data were taken on 15 October 1998 during the CLARE'98 field campaign. Small cells characteristic of altocumulus are apparent in the accompanying photograph from the cloud camera, indicating that the layer is convective in nature. No layer is visible in the accompanying observations by the 35 GHz Rabelais radar at Chilbolton (resolution 75 m and 30 s), since the radar echos at this frequency are dominated by the contribution from the larger ice particles falling beneath the glaciating liquid water cloud. Ice cloud is visible in the photograph as much fainter but more homogeneous wisps beneath the liquid water cells. The radiosonde ascent from Herstmonceux (125 km away) shows that the layer was saturated with respect to liquid water and convectively unstable. The cells in the photograph were around 500 m across, too small to be resolved by the 30 s resolution of the lidar given that the wind speed at this altitude (from the radiosonde ascent) was 26 m s^{-1}. Heymsfield et al. (1991) presented aircraft measurements of liquid water in two altocumulus clouds and demonstrated using a numerical model that the observations were consistent with radiatively-driven convective overturning.

Spaceborne lidar and radar would be ideally suited the task of detecting the presence of supercooled layers on a global basis, and would have the important advantage of viewing from above and thus avoiding the problem of extinction by low cloud. Figure 2.12 illustrates this point with observations by an airborne 1064 nm nadir-pointing polarisation lidar in the vicinity of Chilbolton. The lidar was mounted on the DLR Falcon aircraft, and the data were taken on 20 October 1998 during CLARE'98. A number of strongly-reflective layers are clearly present in the β field, and their low depolarisation indicates that they are composed predominantly of spherical water droplets. Simultaneous measurements by the scanning 3 GHz Chilbolton radar show no such features in reflectivity (Z), but do show unusually high values of differential reflectivity (Z_{DR}), indicating the presence of horizontally-aligned, highly non-spherical crystals falling beneath the supercooled water layers (Hogan et al. 1999). In situ measurements by the UK Met Office C-130 aircraft at an altitude of around 4 km ($-7°$C) revealed the lowest elevated lidar echo to be associated with liquid water contents of up to around 0.2 g m^{-3}. The vertical velocity at this altitude and more than 25 km from Chilbolton exhibits a clear periodicity with an amplitude of around 0.6 m s^{-1} and a wavelength of around 15 km, indicating that a gravity wave was probably responsible for the updrafts that caused the supercooled liquid water to condense. From the horizontal wind speed of 18 m s^{-1} we calculate that a parcel affected by the gravity wave is vertically displaced by ± 80 m, and its temperature correspondingly varies by around ± 0.6 K. The saturation vapour density would therefore vary by ± 0.13 g m^{-3}, which is very much in line with the liquid water contents observed at the crests of each wave beyond 25 km. Lidar ceilometer observations on this day (not shown) could not penetrate the lowest of

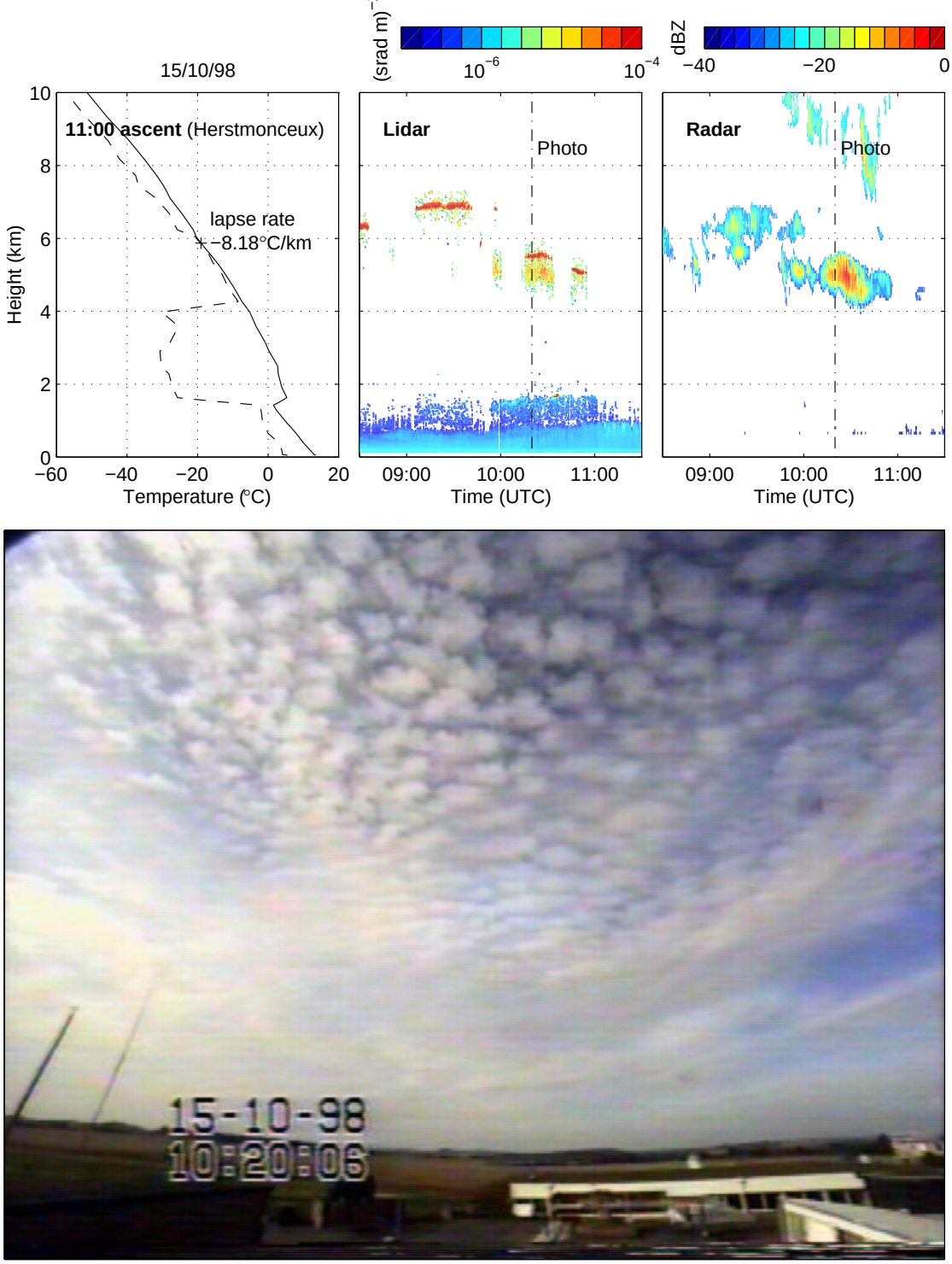

Figure 2.11: Time-height section of lidar backscatter coefficient and 35 GHz radar reflectivity through a supercooled layer, with a simultaneous photograph from the cloud camera. The radiosonde dry-bulb and dew-point temperature profile measured at Herstmonceux is also shown. The data were taken on 15 October 1998 at Chilbolton.

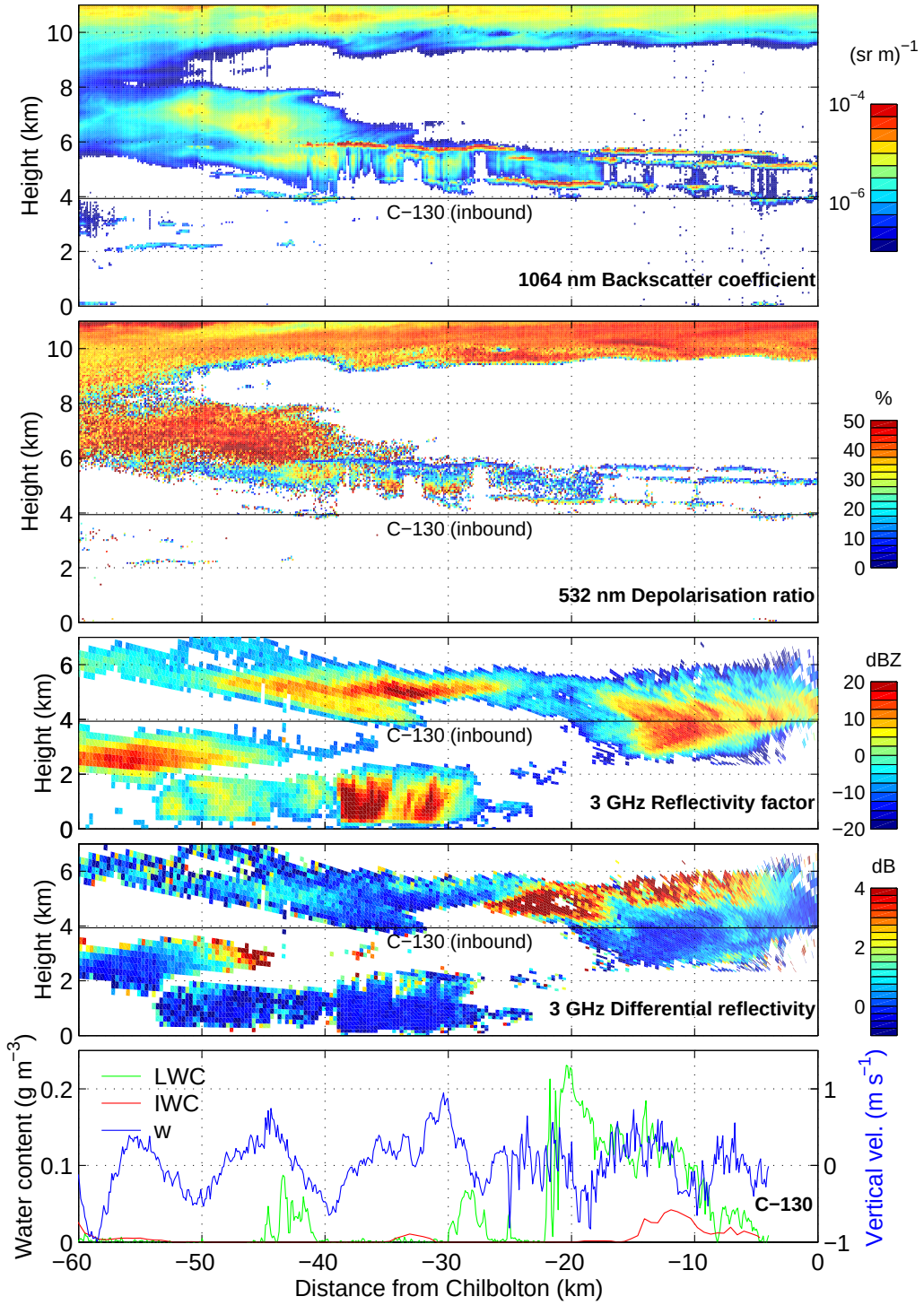

Figure 2.12: Composite of observations from the run at 1420 on 20 October 1998 during CLARE'98. The first two panels show measurements by the nadir-pointing lidar on board the Falcon aircraft flying at an altitude of 13 km. Simultaneous measurements of Z and Z_{DR} by the ground based 3 GHz radar at Chilbolton are shown in the next two panels, and the last shows liquid water content, ice water content and vertical velocity measured by the C-130 aircraft at an altitude of 4 km ($-7°$C).

In the remainder of this section, several years of observations by a 905 nm Vaisala CT75K lidar ceilometer are analysed to estimate the frequency of occurrence of supercooled liquid water layers as a function of temperature. It is found that they are much more common than one might suppose, highlighting the need for further measurements on a global basis. To examine the effect of specular reflection by planar ice crystals to produce layers of high β that anomalously register as supercooled water, we also examine data from a Vaisala lidar ceilometer operating at 5° from zenith.

2.5.2 Objective identification of layers from ceilometer data

Layers can be identified easily by eye from time-height sections of β, so the first step is to automate the process of layer identification using a set of fixed rules. The data acquisition system from the Vaisala instrument outputs the height of the first cloud base (h) in addition to the β profile. It calculates h by performing a so-called Klett inversion of the β profile assuming a fixed extinction-to-backscatter ratio, and considers the slope, absolute value and historic observations at that height. The base of liquid water clouds (both at temperatures above and below 0°C) are characterised by high values of β above a sharp gradient in β, and comparison of h with the β profile indicates that supercooled layers identified subjectively *always* coincide with the first cloud base. However, when no liquid water cloud is present, h is unreliable.

Hence we use h as the starting point for automatic layer identification, and do not attempt to identify more than one layer in each ray. Firstly, the height of the maximum β within 150 metres of h is found. Two tests are then applied that have been found to give best agreement with layers identified subjectively: a layer of supercooled water should have a value of β greater than 4×10^{-5} sr^{-1} m^{-1} and this peak value should be at least 20 times greater than the value 300 m (10 range gates) above. Two examples of layer identification using this simple algorithm are shown in Fig. 2.13. In the first case the supercooled water occurs at around -8°C and is embedded within a more extensive ice cloud. The longevity of the layer despite the presence of ice is rather difficult to explain, and highlights the need for further case studies involving in situ measurements and cloud resolving model simulations. The second case shows a more typical altocumulus cloud topped by a layer of liquid water. In both cases the algorithm has successfully located the position of the layer. An algorithm based purely on the maximum value of β was tried, but it was found that very cold layers could be missed while reflective clouds that were not layer-like in appearance, such as the lower parts of deep cirrus, tended to be included.

Radiosonde data was used to estimate the temperature at the altitude of the layer. The nearest operational upper-air station to Chilbolton is Herstmonceux, 125 km away, which carries out ascents every six hours. This station is used in preference to the so-called ‘range’ station at Larkhill, which is only 25 km away but does not perform regular ascents. Linear interpolation was performed in both time and height, but there is likely to be a residual error of several degrees in the derived temperature profile over Chilbolton.

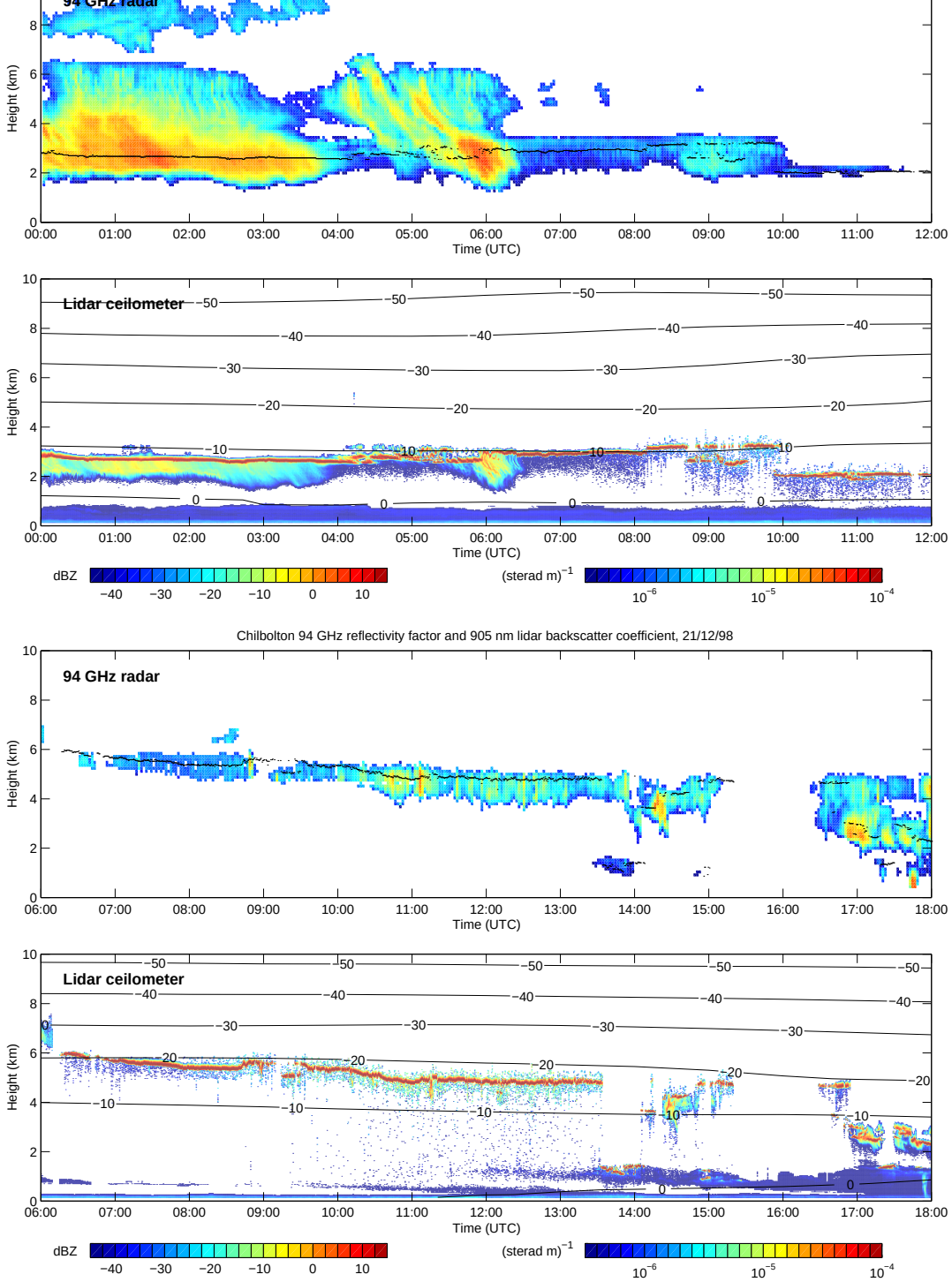

Figure 2.13: Two examples of the objective layer-identification scheme, from Chilbolton on 23 November and 21 December 1998. The top panel for each day shows a time-height section of radar reflectivity from the 94 GHz Galileo radar at Chilbolton (resolution 2 minutes and 120 metres). Superimposed are black points indicating the presence of a layer, derived from the ceilometer data which is shown in the lower panel for each day (resolution 30 seconds and 30 metres). Also shown is temperature according to the ECMWF model.

The algorithm has been applied to all the ceilometer data taken at Chilbolton, from when the instrument was installed in the summer of 1996 until April 1999. Some data is missing, particularly in the first five months, but in total 2.47 million 30-second rays have been processed, equivalent to over 28 continuous months of observations.

We first consider the dataset as a whole to estimate the occurrence of supercooled layers as a function of temperature. The results are summarised in Fig. 2.14. Panel (a) shows the fraction of the dataset for which the instrument observed any cloud in each 5° temperature interval between −50°C and −5°C. Pixels were defined to be cloudy if the lidar backscatter coefficient was at least 2×10^{-7} $\mathrm{sr}^{-1}\,\mathrm{m}^{-1}$. At temperatures warmer than −5°C the data were often contaminated by aerosol so are not shown. A method was devised to 'clean-up' the clear-air noise occasionally produced by this instrument. It can be seen that the occurrence of cloud in each 5° bin was less than 10% and decreased with decreasing temperature. This will be appreciably less than the true cloud occurrence, because of the problem of obscuration by lower level clouds at lidar wavelengths.

Panel (b) shows the fraction of clouds that contained a layer satisfying the definition given earlier, in each 5° interval. As one might expect, the fraction of clouds containing a supercooled layer decreases with temperature; 18.5% of clouds between −10°C and −15°C contained a supercooled layer, whereas between −30°C and −35°C the value falls to only 5.5%. The lower two panels depict similar information but in a cumulative sense. Panel (d) shows the fraction of observations with clouds colder than a given temperature that contained a layer colder than this temperature. We see that around 30% of the time that cloud colder than −10°C was observed, a layer was observed within it, falling to 20% when considering only clouds colder than −20°C.

Figure 2.15 shows the mean layer duration and horizontal extent as a function of temperature. Horizontal extent was calculated from layer duration using the wind speed at that height as given by the interpolated radiosonde profile. Because of the frequent temporary obscuration of the layers by passing low level cumulus, layers were deemed continuous in this analysis provided any gaps in them lasted no longer than 10 minutes. We see that at −5°C the average layer persisted for over half an hour, with the average duration falling steadily with decreasing temperature. Typical horizontal extents were between 20 and 30 km, although because of obscuration this is likely to be a considerable underestimate. Figure 2.13 shows cases in which layers were observed to persist for much longer.

An attempt was made to estimate the optical depth of these layers by performing a simple Klett-type inversion on each profile to remove the effects of attenuation. An extinction-to-backscatter ratio suitable to liquid water of 15 sr was employed. However, all gate-by-gate procedures for correcting attenuated backscatter profiles are potentially unstable and very sensitive to both instrument calibration and the chosen extinction-to-backscatter ratio, and indeed our retrieved optical depths calculated by this method were often impossibly large. The mean optical depth of those layers for which the procedure did not explode was around 0.2, but given the problems with this technique it is doubtful that this value is accurate. The apparent physical thickness of the high β region was typically around 150 metres (5 range gates), but because of the strong attenuation the true thickness is likely to be much greater.

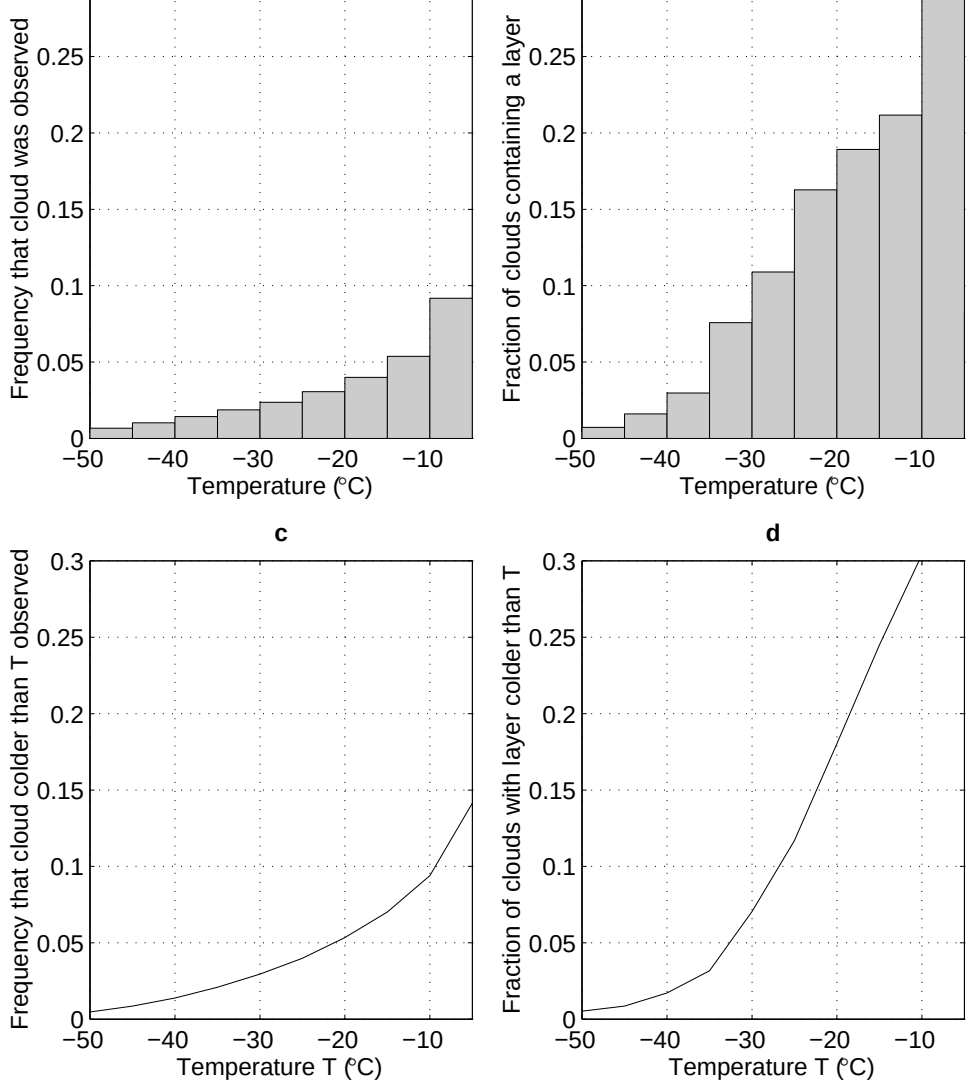

Figure 2.14: Statistics from the 31-month zenith-pointing lidar ceilometer dataset taken at Chilbolton, England: **(a)** Fraction of observations in which cloud was seen in each 5° temperature range; **(b)** Fraction of clouds that contain a layer in each 5° temperature range; **(c)** Fraction of observations in which a cloud colder than a given temperature is observed; **(d)** Fraction of clouds colder than a given temperature that contain a layer.

We next divided the dataset into months to look for any seasonal or longer-term trend. A few months had too little time in which the ceilometer was operating to produce robust statistics, so have been rejected from this analysis. The remaining 31 months all have data equivalent to more than 15 continuous days of observations, and the average is equivalent to 27.7 continuous days. Figure 2.16 shows the fraction of clouds in three different 10° temperature intervals that contain a supercooled layer, as a function of time. We use 10° rather than 5° intervals in an attempt to reduce scatter. No robust seasonal or other trend is obvious, but in any case the dataset can only really be considered continuous from February 1997, and it appears that 2 years is not sufficient to reveal any trend if one exists.

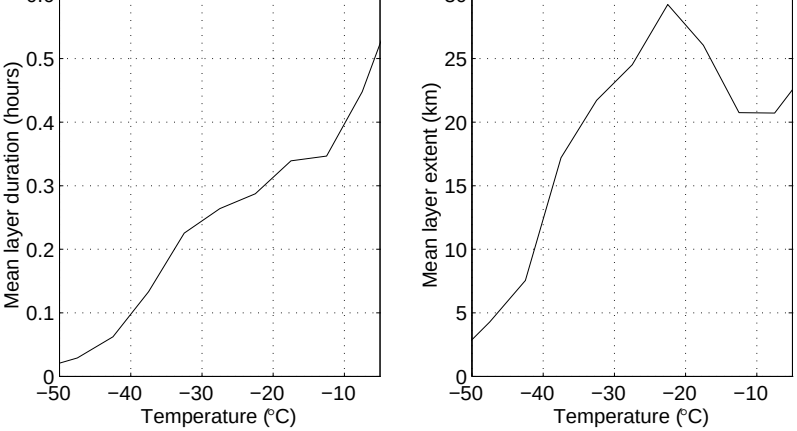

Figure 2.15: Mean duration and horizontal extent of individual layers versus temperature.

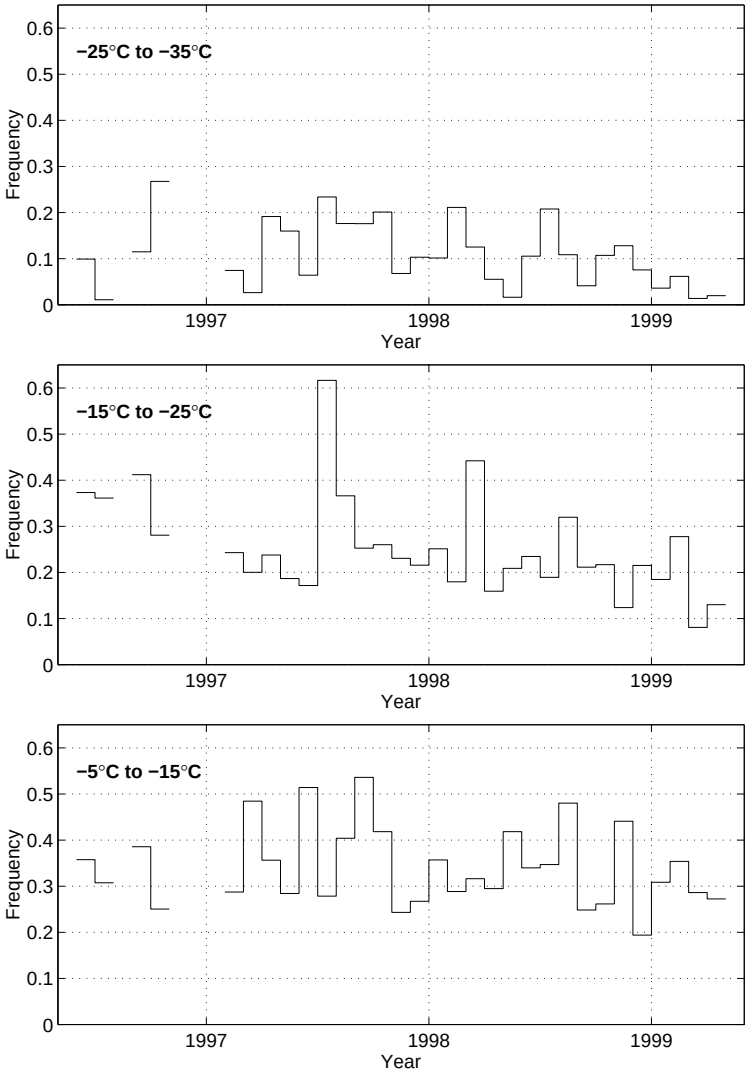

Figure 2.16: Frequency of supercooled layers in three different temperature ranges, for individual months.

the magnitude of which was seen to fall rapidly as the lidar pointing angle was moved a little away from zenith. This was interpreted as being due to specular reflection from horizontally-aligned plate crystals. Throughout the period of observation by the ceilometer at Chilbolton, the instrument was operating in a zenith-pointing configuration, so could be affected. This could be the reason that the fraction of clouds containing a layer does not fall quite to zero at $-40°$C, where because of homogeneous nucleation no supercooled water should exist (Fig. 2.14b). Visual examination of the ceilometer data on such occasions suggests these events are aircraft contrails, which due to the large numbers of aerosols present tend to consist of high concentrations of very small ice crystals, so can understandably be mistaken for layers of liquid water. Indeed, Fig. 2.15 indicates that clouds identified as supercooled layers that are colder than $-40°$C persist on average for only three minutes. It is also possible that the temperature calculated by interpolating radiosonde profiles could be in error by in excess of $5°$. In any case, layers colder than $-40°$C were diagnosed for only 4.9 hours of the 28 months of observations, corresponding to only 0.024% of the dataset. In the next section we apply the algorithm to data from a ceilometer operating a few degrees from zenith to eliminate the effect of specular reflection.

It would seem fairly safe to assume that the layers observed by the airborne lidar in Fig. 2.12 were composed primarily of liquid water droplets because of the low lidar depolarisation and the in situ verification. The radiosonde profile in Fig. 2.11 strongly suggests that the layer in this example is composed of liquid water. One striking property of these layers is that they tend to completely extinguish the lidar signal (see Fig. 2.13 for an example), whereas specular reflection from plates is only an enhancement of the backscatter, and the extinction should remain largely unchanged. Certainly the clouds observed by Thomas et al. (1990) did not strongly attenuate the lidar signal, although unfortunately absolute values of β were not quoted. An apparent layer was observed on 21 October 1998 during CLARE'98 at a temperature of around $-20°$C that had a high depolarisation ratio (indicating ice crystals) and according to the in situ measurements did not contain significant liquid water.

2.5.4 Statistics from a ceilometer operating at $5°$ from zenith

To test whether specular reflection could be affecting the results, 51 days of data from a Vaisala lidar ceilometer operating $5°$ from zenith at Cabau, The Netherlands have been analysed in exactly the same way as the Chilbolton data. The observations were taken between 18 August and 4 November 1999, and radiosonde ascents from De Bilt (25 km to the north east of Cabau) were used. The results are shown in Fig. 2.17, and we see that this time only a tiny fraction of clouds colder than $-35°$C contained a layer, and the occurrence of layers is somewhat less than at Chilbolton for all temperature ranges. This suggests that some of the layers observed in the 31 months of zenith-pointing actually corresponded to specular reflection from ice crystals, particularly at very cold temperatures. However, 51 days are not really sufficient for sound statistics on supercooled layer occurrence, and several years of observations by an off-zenith lidar would be required to confirm these findings.

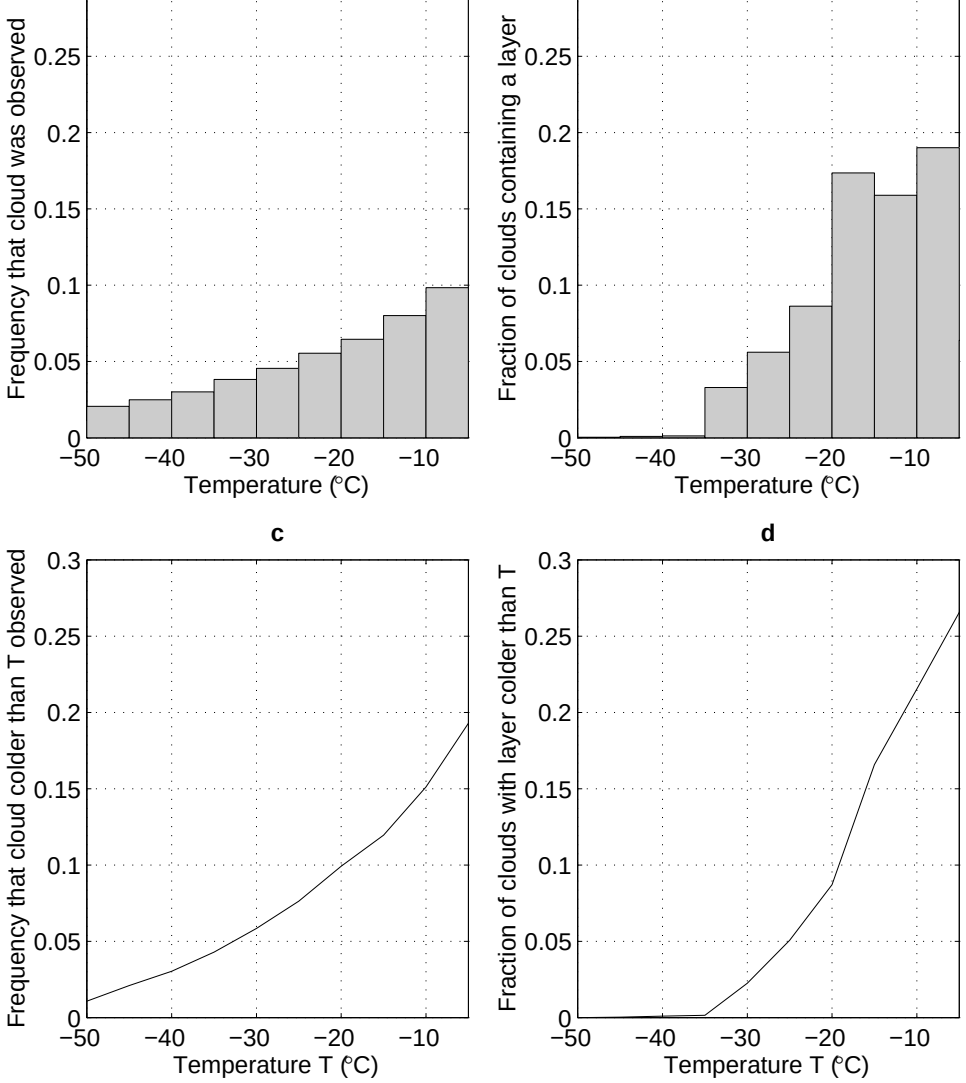

Figure 2.17: Statistics from 51 days of data taken by the off-zenith lidar ceilometer at Cabau, The Netherlands: **(a)** Fraction of observations in which cloud was seen in each 5° temperature range; **(b)** Fraction of clouds that contain a layer in each 5° temperature range; **(c)** Fraction of observations in which a cloud colder than a given temperature is observed; **(d)** Fraction of clouds colder than a given temperature that contain a layer.

2.5.5 Conclusions and future work

Lidar ceilometer data has been analysed in a first attempt to characterise the frequency of supercooled layer clouds as a function of temperature. From a 31-month dataset it is found that they occur surprisingly often; 30% of the time that the lidar sees cloud colder than $-10°C$ it also sees a layer colder than this. Given that they are much more radiatively important than any ice at the same altitude, and their role in glaciation and precipitation processes, it is important that some attempt is made to represent them properly in forecast and climate models. It would appear that a simple fixed ratio between ice and liquid water as a function of temperature is too crude if the radiative properties of sub-freezing clouds are to be

Analysis of a much shorter dataset measured by a lidar ceilometer operating at a few degrees from zenith suggested that the few layers that were observed at temperatures below $-35°C$ in fact corresponded to specular reflection from the crystals in purely ice clouds. Longer periods of observation with an off-zenith lidar are clearly required to derive robust statistics on the occurrence of supercooled layers while avoiding contamination of the data by specular reflection. Even the 31-month dataset was not long enough for any seasonal or interannual trends to be evident, so it would be interesting to repeat the procedure for even longer periods and at a number of different sites. It would also be useful to investigate whether the occurrence of supercooled layers can be correlated with any large scale model field that could be used as the basis for a parameterisation. Clearly the proposed spaceborne lidar could play a crucial role in gathering data on supercooled clouds on a global basis, and much would be learned by combining β with simultaneous measurements of radar reflectivity and lidar depolarisation.

2.6.1 Introduction

The distribution of clouds in the atmosphere represents one of the major uncertainties in our understanding of the present climate (IPCC 1995), and limits our confidence in future climate prediction. General Circulation Models (GCMs) currently carry a value for cloud fraction in each model gridbox but it has been found that different assumptions on the way clouds overlap in a vertical column of gridboxes can have a strong effect on the model radiation budget (Morcrette and Fouquart 1986, Charnock et al. 1994, Liang and Wang 1997, Stubenrauch et al. 1997). This in turn affects circulation patterns (Liou and Zheng 1984, Slingo and Slingo 1988, Randall et al. 1989). The three different cloud overlap assumptions that have commonly been made in GCMs are shown schematically in Fig. 2.18. Integrations of the European Centre for Medium-Range Weather Forecasts (ECMWF) model by Morcrette and Jakob (2000) highlighted the important differences between them: simulated global-mean cloud cover was 71.4% when random overlap was assumed but only 60.9% in the case of maximum overlap, and over parts of the ITCZ the resulting differences in mean outgoing longwave radiation were in excess of 40 W m^{-2}. While the importance of cloud overlap for radiation has long been recognised, it is only recently that its role in determining the efficiency of precipitation formation has also been studied (Jakob and Klein 1999).

Nearly all GCMs now employ the so-called 'maximum-random' overlap assumption, whereby vertically continuous clouds are assumed to be maximally overlapped while clouds at different heights that are separated by an entirely cloud-free model level are randomly overlapped (Geleyn and Hollingsworth 1979). The passive observational data used to support this approach has so far been very limited in vertical resolution (Tian and Curry 1989). Barker et al. (1999) carried out Monte Carlo simulations of

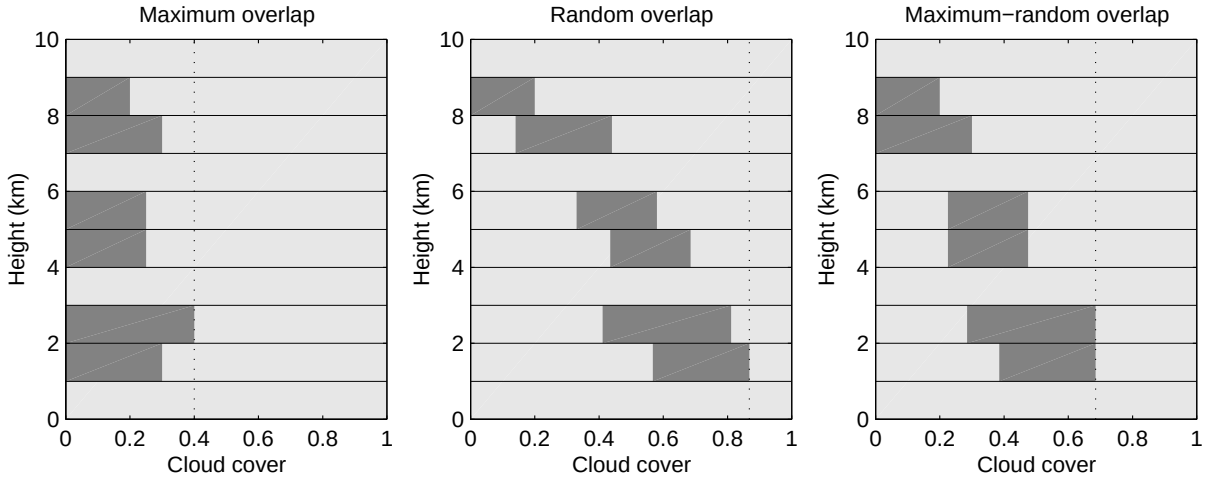

Figure 2.18: A schematic illustrating the three overlap assumptions that are commonly made in GCMs. The dotted vertical lines denote total cloud cover. For clarity we have adopted the convention used by Morcrette and Jakob (2000) and drawn only a single cloud at each level. While the total cloud cover from the top of the atmosphere down to any particular level is correct, the use of a single cloud at each level in the diagram is a simplification for the overlap of any two individual layers in the cases of random and maximum-random overlap.

flux differences of up to 100 W m^{-2}. They looked forward to a time when overlap could be validated from ground-based and spaceborne radars.

The potential of ground-based high vertical resolution radars for the validation of model cloud occurrence was first demonstrated by Mace et al. (1998), and more recently the actual values of cloud fraction in ECMWF model gridboxes were validated using radar (Illingworth et al. 1999, Hogan et al. 2000b). It was found that the ECMWF model exhibited a good degree of skill in predicting cloud fraction; Fig. 2.19 shows a comparison of cloud fraction from the model and the observations for a ten-day period. In this section we report new results on cloud overlap derived using the same dataset as was used by Hogan et al. (2000b). In contrast to the findings for cloud fraction, it is found that true cloud overlap is not well represented by the ubiquitous maximum-random assumption, a result which could have serious implications for the radiation budgets of the models that use it. The technique we describe would be an ideal application for the proposed spaceborne radar, and would allow the overlap characteristics of clouds to be measured globally.

2.6.2 Method

We use the near-continuous observations taken between 6 November 1998 and 24 January 1999 by the ESTEC 94-GHz 'Galileo' radar at Chilbolton, England. The radar was vertically-pointing and recorded radar reflectivity factor (Z) as a 10-s average with a vertical resolution of 60 m. A 6.9 dB increase in sensitivity was achieved by averaging over 2 mins and 120 m, resulting in minimum-detectable Z of around -52.5 dBZ at 1 km and -32.5 dBZ at 10 km. The clouds most likely to be undetected by radar are high thin cirrus, but it was shown by Brown et al. (1995) that virtually all 'radiatively-significant' cirrus (essentially that which decreases outgoing longwave radiation by at least 10 W m^{-2}) should be detected by a radar with a minimum-detectable Z of -30 dBZ. A reduction in the sensitivity of the instrument by 5 dB is found to have a negligible effect on the final results, so there is no reason to suppose that very tenuous clouds should have significantly different overlap characteristics from detectable clouds. Nonetheless, we restrict our analysis to data recorded below 10.5 km. Data below 750 m are not used because here the radar sensitivity is somewhat compromised by leakage of the transmit pulse into the receiver. It should be noted that the common problem of data contamination by insects is entirely absent at the latitude of Chilbolton during winter.

To compute actual overlap, daily time-height sections of Z were divided into equally-sized boxes, and within each box a simple 'cloud cover mask' was generated consisting of 'bits' stating whether or not cloud was present at any height within the box in each 2-minute period. To mimic the range of vertical and horizontal resolutions of current GCMs, box sizes of 360 m, 720 m, 1080 m and 1440 m in the vertical and 20 mins, 1 hour and 3 hours in time were used. Taking the mean tropospheric horizontal wind speed to be 20 m s^{-1} (estimated from ECMWF model data over Chilbolton during the experimental period), these temporal resolutions translate to horizontal distances of 24 km, 72 km and 216 km respectively, spanning the range of horizontal resolutions used by operation mesoscale models to climate models. Cloud cover (c) was then defined as the fraction of bits in each box that were cloudy. An example of the generation of the cloud cover mask from a 12-hour time-height section of Z is shown in

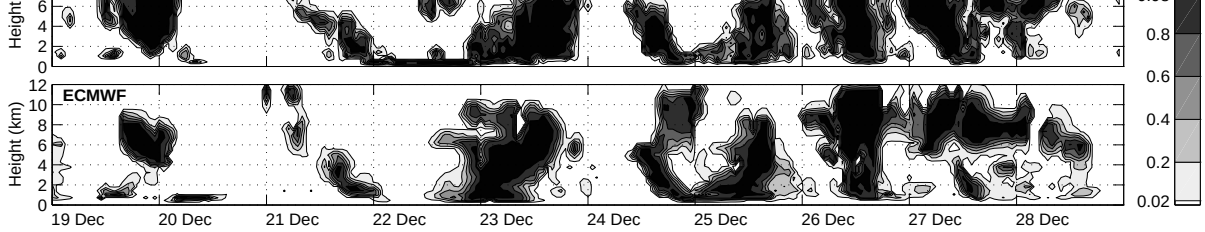

Figure 2.19: Comparison of observed and ECMWF model cloud fraction at Chilbolton for a ten-day period in 1998.

Fig. 2.20. It might initially appear that a vertical column of gridboxes with 100% cloud cover at every level is indicative of maximum overlap, but in fact nothing can be inferred about overlap when one or more of the levels under consideration is completely cloudy, since all overlap assumptions must predict the same total cloud cover: 100%. From the vertically continuous cloud enclosed by the red box between 18 and 19 UTC, it can be seen immediately that as levels further and further apart are considered, maximum overlap becomes an increasingly poor assumption.

In order to quantify this effect, levels were analysed in pairs, with every possible combination of levels being considered, and no 'double-counting'. For each pair, four possible values for the combined cloud cover (C) of the two levels were calculated. The first was the combined cloud cover obtained assuming random overlap, using the standard definition

$$C_{\text{rand}} = c_{\text{a}} + c_{\text{b}} - c_{\text{a}}c_{\text{b}} \tag{2.10}$$

(where c_{a} and c_{b} are the cloud covers of the lower and upper levels respectively), the second was the value obtained assuming maximum overlap, defined as

$$C_{\text{max}} = \max(c_{\text{a}}, c_{\text{b}}), \tag{2.11}$$

the third was the value obtained assuming minimum overlap, defined as

$$C_{\text{min}} = \min(1, c_{\text{a}} + c_{\text{b}}), \tag{2.12}$$

and the fourth was the combined cloud cover that was actually observed, C_{true}. Note that the subscript 'max' corresponds to the maximum *overlap* and not the maximum possible C; in fact C_{max} is the *minimum* possible value of C (see Fig. 2.18). Pairs in which either of the levels had a cloud cover of zero or unity were rejected, as in these cases all values of C are equal. Hence after averaging over a sufficiently large number of events, the position of the observed $\overline{C}_{\text{true}}$ between $\overline{C}_{\text{max}}$ and $\overline{C}_{\text{rand}}$ (as a function of level separation) will tell us precisely how a radiation scheme ought to weight cloud overlap between the two extremes of maximum and random.

A problem to consider when deriving overlap at 94 GHz is attenuation by liquid water; when heavy rain is present at low levels the radar beam can be completely obscured, resulting in vertical swaths of apparently cloud-free air directly above the rain. This has the effect of increasing the apparent overlap since the erroneously cloud-free regions are stacked on top of each other. We therefore use measurements taken by a drop-counting rain gauge at Chilbolton to reject from the analysis all events for which the rain

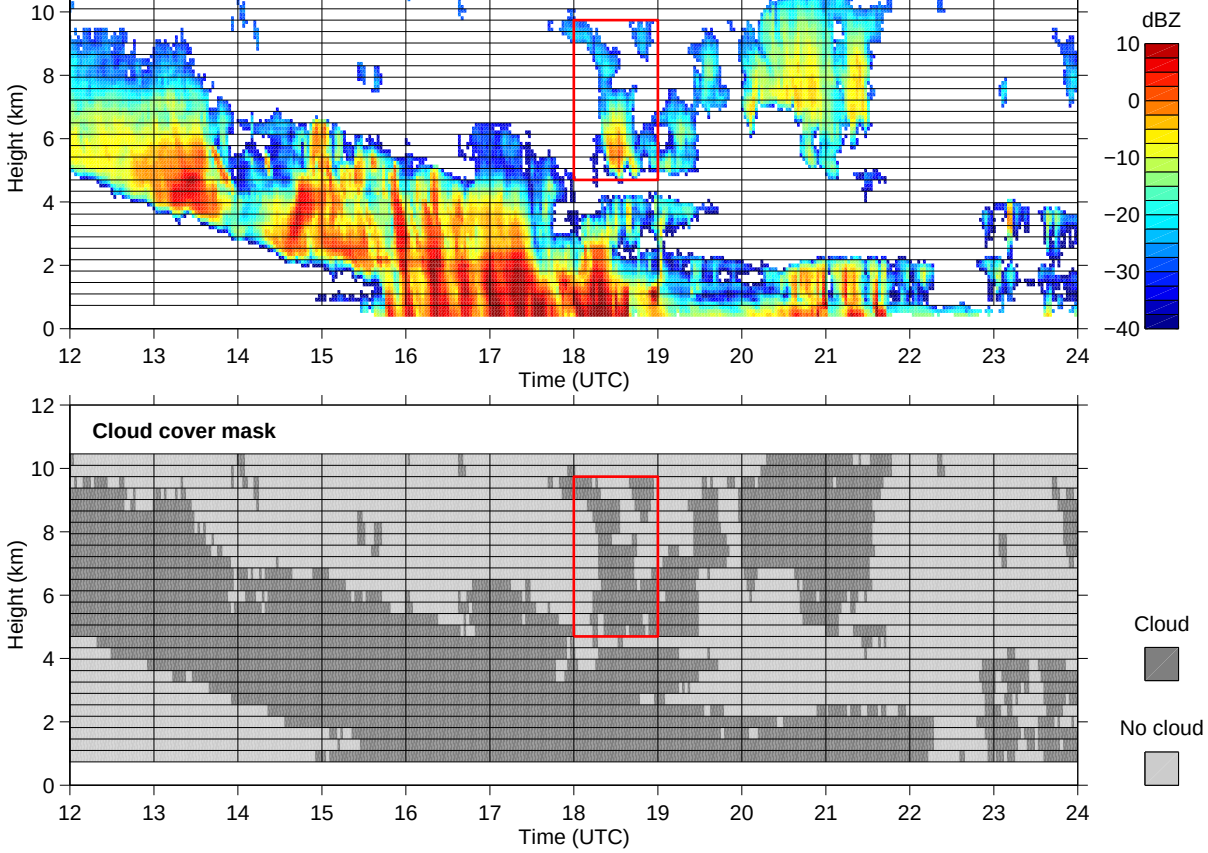

Figure 2.20: An example of cloud radar data used to derive the cloud cover mask, from 11 December 1998. Intermittent light drizzle was measured at the ground between 17 and 19 UTC. The resolution of the grid is 360 m and 1 hour.

rate exceeded 0.5 mm hr^{-1} at any time during the sample period. The effect on the derived overlap characteristics was small because less than 10% of the data were removed in this way. The effect of drizzle falling beneath liquid water clouds was investigated by restricting the analysis to regions where the temperature was below 0°C: the change in the overlap statistics was negligible. Another possibility is that large but radiatively-unimportant snow crystals falling beneath ice clouds could be detected by the radar and bias the results. Analysis of simultaneous radar and lidar returns from ice clouds at all heights by Hogan and Illingworth (1999a) revealed that this is a rare occurrence; in 94% of their data the radar and lidar cloud base agreed to within 360 m (the highest vertical resolution considered in the present study).

2.6.3 Results

The results for boxes measuring 360 m by 1 hour are shown in Fig. 2.21. Pairs of levels have been grouped together according to their vertical separation, but separated according to whether they are vertically continuous (i.e. the cloud cover in every interstitial level is greater than zero) or non-continuous. We see that in the case of vertically continuous cloud, as the level separation is increased from 360 m

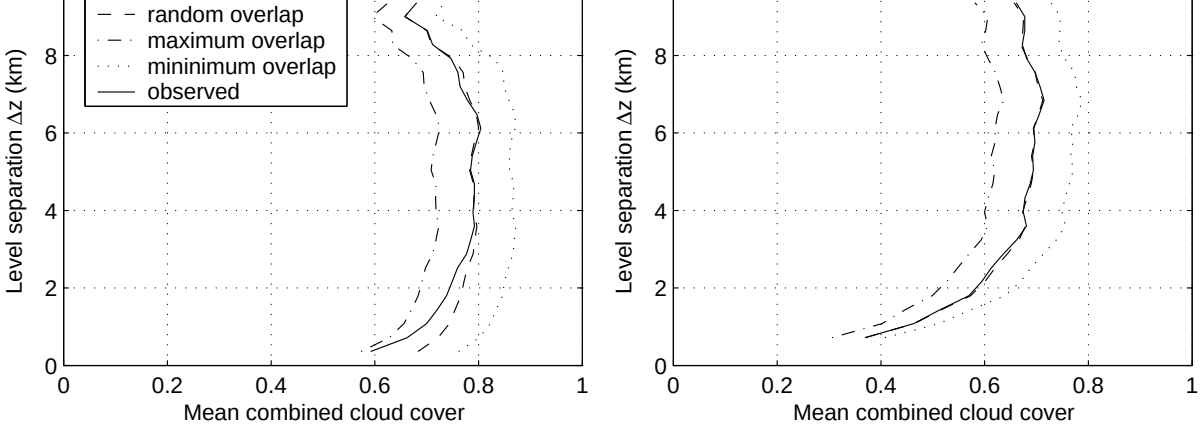

Figure 2.21: The mean observed combined cloud cover of pairs of levels as a function of level separation (solid line), together with the values calculated using three different overlap assumptions. The vertical resolution was 360 m and the temporal resolution was 1 hour. Only events where the cloud cover at both levels was greater than zero and less than one were used. The left panel was compiled from events for which every intermediate level contained some cloud and the right panel corresponds to cases for which at least one of the intermediate levels was entirely cloud-free.

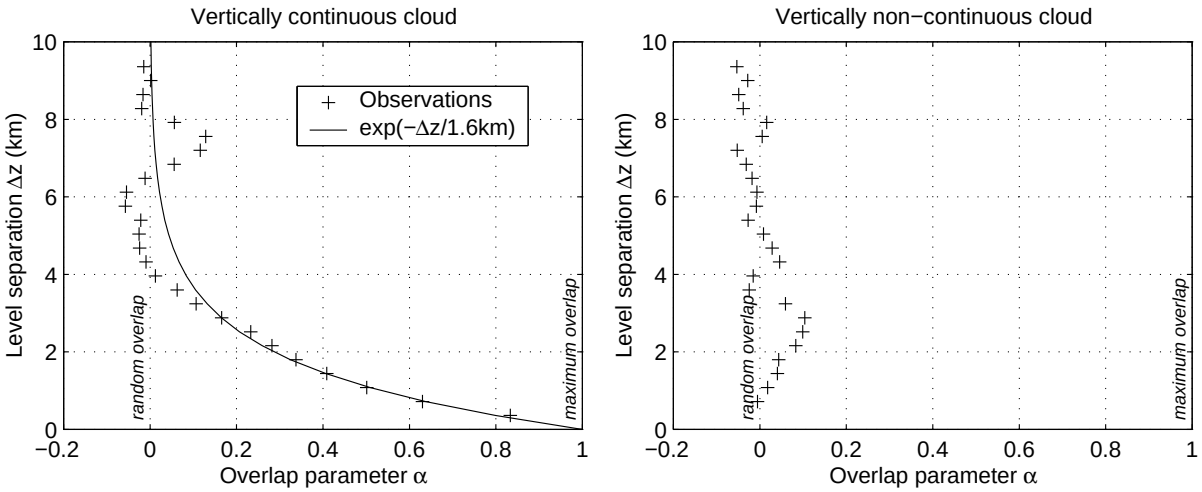

Figure 2.22: The overlap parameter α versus level separation for vertically continuous and non-continuous cloud, using boxes 360 m in height and 1 hour in duration. A value of unity indicates maximum overlap and a value of zero indicates random overlap.

to 4 km, $\bar{C}_{\text{true}}$ moves from a value close to that calculated assuming maximum overlap, to essentially the random overlap value. This contrasts with most current GCMs which apply maximum overlap to all vertically continuous levels. In the case of vertically non-continuous cloud on the other hand, there appears to be no significant deviation of $\bar{C}_{\text{true}}$ from that predicted assuming random overlap, in agreement with the schemes used in most GCMs. Of course in individual cases C_{true} takes values anywhere between the extremes of C_{max} and C_{min}.

A simpler and more useful way of presenting these findings is in terms of an 'overlap parameter' α that

360 m	1.40 km	1.60 km	2.04 km
720 m	1.68 km	1.90 km	2.30 km
1080 m	2.04 km	2.15 km	2.48 km
1440 m	2.54 km	2.56 km	2.93 km

Table 2.1: Values of the e-folding distance Δz_0 for different vertical and temporal resolutions.

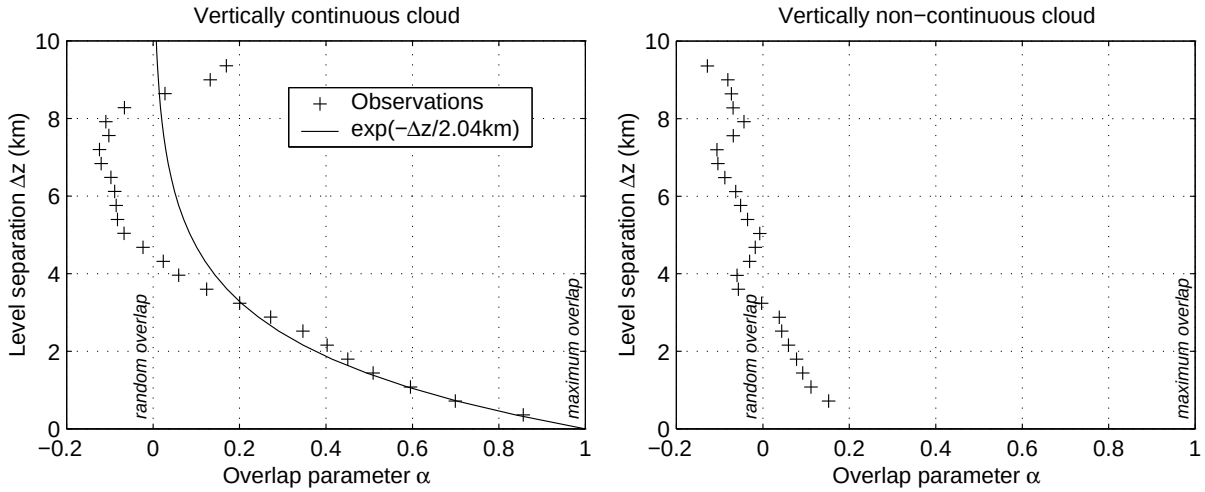

Figure 2.23: The overlap parameter α versus level separation for vertically continuous and non-continuous cloud, using boxes 360 m in height and 3 hour in duration.

expresses $\bar{C}_{\text{true}}$ in terms of $\bar{C}_{\text{max}}$ and $\bar{C}_{\text{rand}}$:

$$\bar{C}_{\text{true}} = \alpha \bar{C}_{\text{max}} + (1-\alpha)\bar{C}_{\text{rand}}. \tag{2.13}$$

Hence $\alpha = 0$ corresponds to random overlap and $\alpha = 1$ to maximum overlap. Figure 2.22 depicts α as a function of level separation, again for 360 m and 1 hour resolution. The observed values of α would seem to be best fitted by an inverse-exponential of the form

$$\alpha = \exp\left(-\frac{\Delta z}{\Delta z_0}\right), \tag{2.14}$$

where Δz is the level separation and Δz_0 is an e-folding or 'decorrelation' distance. The value of Δz_0 has been estimated for each of the three temporal resolutions and four vertical resolutions by performing a least-squares fit to the observations, but weighting each observation by the number of events from which the average was calculated. The results are shown in Table 2.1. Hence if cloud overlap were to be parameterised in models using Eq. 2.14 then the value of Δz_0 could be chosen to match the model resolution. The weighting is necessary because cloud frequency obviously decreases with increasing physical thickness, and some possible statistical noise is apparent in α for level separations of more than 7 km. Nonetheless, it is remarkable that as little as a few days of data are sufficient to exhibit essentially the same overlap behaviour as shown in Fig. 2.22, indicating that this 71 day dataset is easily long enough to derive robust values of Δz_0.

It can be seen from Table 2.1 that a decrease in either temporal or vertical resolution results in an increase in Δz_0 and thus an increase in the degree of overlap for a given level separation. The change with temporal

the degree of overlap can never decrease with decreasing temporal resolution. A reduction in vertical resolution can, in individual cases, result in either an increase or a decrease in the degree of overlap, but it simply turns out that the former is more common, particularly for adjacent levels. It is found that Δz_0 does not have a significant dependence on whether the pairs of levels are taken from the upper or lower troposphere. One interesting finding is that with a temporal resolution of 3 hours and a level separation of between 6 and 8 km, α falls to -0.1, indicating a tendency for a lower degree of overlap than even that predicted by the random overlap assumption. This is shown in Fig. 2.23. The reason for this behaviour is that in Southern England during winter, fronts are almost entirely responsible for clouds more than 5 km thick, and these have a characteristic 'slanted' signature in radar time-height sections that can only really be detected in sections of 3 hours or longer. Fig. 2.20 is a striking example of such an event.

2.6.4 Conclusions

A simple method for using long-term radar observations to characterise cloud overlap has been developed that expresses mean overlap in a way that could be implemented in GCMs. It has been found that the mean overlap of vertically continuous clouds is distinctly more random than models usually assume, and this will probably have a significant effect on the predictions made with such models. Before applying the findings of this study to global models it would be advisable to use the technique to derive overlap statistics from cloud radars in other locations, and in all seasons, since the overlap characteristics of convective clouds may be appreciably different from those of frontal clouds. A spaceborne cloud radar would be ideally suited to this task, and simultaneous measurements by the lidar would also be valuable in ensuring that all radiatively significant cloud is detected.

Ansmann, A., U. Wandinger, M. Riebesell, C. Weitkamp and W. Michaelis, 1992: Independent measurement of extinction and backscatter profiles in cirrus clouds by using a combined Raman elastic-backscatter lidar. *Appl. Optics,* **33**, 7113–7131.

Atlas, D., S. Y. Matrosov, A. J. Heymsfield, M.-D. Chou and D. B. Wolff, 1995: Radar and radiation properties of ice clouds. *J. Appl. Meteor.,* **34**(11), 2329–2345.

Auer, A. H., and D. L. Veal, 1970: The dimension of ice crystals in natural clouds. *J. Atmos. Sci.,* **27**, 919–926.

Barker, H. W., G. L. Stephens and Q. Fu, 1999: The sensitivity of domain-averaged solar fluxes to assumptions about cloud geometry. *Quart. J. Roy. Meteor. Soc.,* **125**, 2127–2152.

Bower, K. N., S. J. Moss, D. W. Johnson, T. W. Choularton, J. Latham, P. R. A. Brown, A. M. Blyth and J. Cardwell, 1996: A parametrization of the ice water content observed in frontal and convective clouds. *Quart. J. Roy. Meteor. Soc.,* **122**, 1815–1844.

Brown, P. R. A., and P. N. Francis, 1995: Improved measurements of the ice water content in cirrus using a total-water probe. *J. Atmos. Oceanic Technol.,* **12**(2), 410–414.

Brown, P. R. A., A. J. Illingworth, A. J. Heymsfield, G. M. McFarquhar, K. A. Browning and M. Gosset, 1995: The role of spaceborne millimeter-wave radar in the global monitoring of ice-cloud. *J. Appl. Meteor.,* **34**(11), 2346–2366.

Charnock, T., F. Rose, T. Alberta, G. L. Smith, D. Rutan, N. Manalo-Smith, P. Minnis and B. Wielicki, 1994: Cloud profiling radar requirements: Perspective from retrievals of the surface and atmospheric radiation budget and studies if atmospheric energetics. In *Utility and feasibility of a cloud profiling radar.* Report of the GEWEX Tropical Workshop, 2–29 July 1993, Pasadena, California, IGPO 10, pp. B10–B21.

Danne, O., G. G. Mace, E. E. Clothiaux, X. Dong, T. P. Ackerman and M. Quante, 1996: Observing structures and vertical motions within stratiform clouds using a vertical pointing 94-GHz cloud radar. *Beitr. Phys. Atmosph.,* **69**(1), 229–237.

Donovan, D. P., and A. C. A. P. van Lammeren, 2000: Combined lidar and radar cloud particle effective size retrievals made during CLARA. *Phys. Chem. Earth,* **25**(2), 115–120.

Donovan, D. P., A. C. A. P. van Lammeren, R. J. Hogan, P. N. Francis, J. Testud, J. Pelon, M. Quante and J. W. F. Goddard, 1999: Comparison of lidar/radar ice cloud parameter retrievals with in-situ measurements. *CLARE'98 Final workshop, 13–14 September 1999,* ESA/ESTEC, Noordwijk, The Netherlands, 173–177.

Eberhard, W. L., 1995: Theory for dual-wavelength CO_2 lidar method to distinguish ice, mixed-phase, and water clouds. *J. Atmos. Oceanic Technol.,* **12**, 130–140.

European Space Agency (ESA), 1999: *Earth Radiation Mission.* ESA SP-1233 (3)—The four candidate Earth Explorer Core Missions, ESA/ESTEC, Noordwijk, The Netherlands.

Fowler, L. D., and Randall, D. A., 1996: Liquid and ice cloud microphysics in the CSU general circulation model. 3. Sensitivity to modeling assumptions. *J. Climate,* **9**, 561-586.

Fox, N. I., and A. J. Illingworth, 1997: The potential of a spaceborne radar for the detection of stratocumulus clouds. *J. Appl. Meteor.,* **36**(6), 676–687.

Francis, P. N., A. Jones, R. W. Saunders, K. P. Shine, A. Slingo and Z. Sun, 1994: An observational and

Francis, P. N., P. Hignett and A. Macke, 1998: The retrieval of cirrus cloud properties from aircraft multi-spectral reflectance measurements during EUCREX ’93. *Quart. J. Roy. Meteor. Soc.,* **124**, 1273–1291.

Geleyn, J. F., and A. Hollingsworth, 1979: An economical analytical method for the computation of the interaction between scattering and line absorption of radiation. *Contrib. Atmos. Phys.,* **52**, 1–16.

Gosset, M., and H. Sauvageot, 1992: A dual-wavelength radar method for ice-water characterization in mixed-phase clouds. *J. Atmos. Oceanic Technol.,* **9**, 538–547.

Gregory, D., and D. Morris, 1996: The sensitivity of climate simulations to the specification of mixed phase clouds. *Climate Dynamics,* **12**, 641–651.

Heymsfield, A. J., L. M. Miloshevich, A. Slingo, K. Sassen and D. O’C. Starr, 1991: An observational and theoretical study of highly supercooled altocumulus. *J. Atmos. Sci.,* **48**(7), 923–945.

Hogan, R. J., 1998: *Dual-wavelength radar studies of clouds.* PhD Thesis, University of Reading, UK.

Hogan, R. J., and J. W. F. Goddard, 1999: Calibration of the ground-based radars used in CLARE’98. *CLARE’98 Final workshop, 13–14 September 1999,* ESA/ESTEC, Noordwijk, The Netherlands, 63–67.

Hogan, R. J., and A. J. Illingworth, 1999a: Analysis of radar and lidar returns from clouds: Implications for the proposed Earth Radiation Mission. *CLARE’98 Final workshop, 13–14 September 1999,* ESA/ESTEC, Noordwijk, The Netherlands, 75–80.

Hogan, R. J., and A. J. Illingworth, 1999b: The potential of spaceborne dual-wavelength radar to make global measurements of cirrus clouds. *J. Atmos. Oceanic Technol.,* **16**(5), 518–531.

Hogan, R. J., A. J. Illingworth and P. R. Field, 1999: Polarimetric radar observations of the growth of highly-aligned ice crystals in the presence of supercooled water. *CLARE’98 Final workshop, 13–14 September 1999,* ESA/ESTEC, Noordwijk, The Netherlands.

Hogan, R. J., A. J. Illingworth and H. Sauvageot, 2000a: Measuring crystal size in cirrus using 35- and 94-GHz radars. *J. Atmos. Oceanic Technol.,* **17**(1), 27–37.

Hogan, R. J., C. Jakob and A. J. Illingworth, 2000b: Comparison of ECMWF cloud fraction with radar derived values. *J. Appl. Meteor.,* in press.

Illingworth, A. J., R. J. Hogan and J. W. F. Goddard, 1999: *Study and measurement of cloud characteristics.* Final report, ESTEC Contract 10568/93/NL/NB.

Intrieri, J. M., G. L. Stephens, W. L. Eberhart and T. Uttal, 1993: A method for determining cirrus cloud particle sizes using lidar and radar backscatter techniques. *J. Appl. Meteor.,* **32**(6), 1074–1082.

Jakob, C., and S. A. Klein, 1999: The role of vertically varying cloud fraction in the parametrization of microphysical processes in the ECMWF model. *Quart. J. Roy. Meteor. Soc.,* **125**, 941–965.

Liang, X.-Z., and W. C. Wang, 1997: Cloud overlap effects on general circulation model simulations. *J. Geophys. Res.,* **102**, 11 039–11 047.

Liao, L., and K. Sassen, 1994: Investigation of relationships between K_α-band radar reflectivity and ice and liquid water content. *Atmos. Res.,* **34**, 299–313.

Liebe, H. J., 1985: An updated model for millimeter-wave propagation in moist air. *Radio Science,* **20**(5), 1069–1089.

Liou, K.-N., and Q. Zheng, 1984: A numerical experiment on the interactions of radiation, clouds and dynamical processes in a general circulation model. *J. Atmos. Sci.,* **41**, 1513–1535.

Liu, C.-L. and A. J. Illingworth, 2000: Towards more accurate retrievals of ice water content from radar measurement of clouds. *Accepted J. Appl. Meteorol*.

Mace, G. G., C. Jakob and K. P. Moran, 1998: Validation of hydrometeor occurrence predicted by the ECMWF using millimeter wave radar data. *Geophys. Res. Let.,* **25**(10), 1645–1648.

Macke, A., J. Mueller and E. Raschke, 1993: Scattering of light by polyhedral ice crystals. *Appl. Opt.,* **32**, 2780–2788.

Matrosov, S. Y., 1993: Possibilities of cirrus particle sizing from dual-frequency radar measurements. *J. Geophys. Res.,* **98**(D11), 20 675–20 683.

Matrosov, S. Y., 1997: Variability of microphysical parameters in high-altitude ice clouds: Results of the remote sensing method. *J. Appl. Meteor.,* **36**(6), 633–648.

McClatchey, R. A., R. W. Fenn, J. E. A. Selby, F. E. Volz and J. S. Garing, 1972: Optical properties of the atmosphere (3rd. ed.), Air Force Cambridge Research Laboratories, Rep. No. AFCRL72-0497, L. G. Hanscom Field.

Mead, J. B., R. E. McIntosh, D. Vandemark and C. T. Swift, 1989: Remote sensing of clouds and fog with a 1.4-mm radar. *J. Atmos. Oceanic Technol.,* **6**, 1090–1097.

Meneghini, R., and L. Liao, 1996: Comparisons of cross-sections for melting hydrometeors as derived from dielectric mixing formulas and a numerical-method. *J. Appl. Meteor.,* **35**(10), 1658–1670.

Morcrette, J. J., and Y. Fouquart, 1986: The overlapping of cloud layers in shortwave radiation parameterization. *J. Atmos. Sci.,* **43**, 321–328.

Morcrette, J.-J., and C. Jakob, 2000: The response of the ECMWF model to changes in cloud overlap assumption. *Mon. Weath. Rev.,* **128**(6), 1707–1732.

Moss, S. J., and D. W. Johnson, 1994: Aircraft measurements to validate and improve numerical model parametrizations of ice to water ratio in cloud. *Atmos. Res.,* **34**, 1–25.

Randall, D. A., Harshvardhan, D. A. Dazlich and T. G. Corsetti, 1989: Interactions among radiation, convection and large-scale dynamics in a general-circulation model. *J. Atmos. Sci.,* **46**(13), 1943–1970.

Sassen, K., 1991: Aircraft-produced ice particles in a highly supercooled altocumulus cloud. *J. Appl. Meteor.,* **30**(6), 765–775.

Sassen, K., C. J. Grund, J. D. Spinhirne, M. M. Hardesty and J. M. Alvarez, 1990: The 27–28 Ocober 1986 FIRE IFO Case Study: A five lidar overview of cloud structure and evolution. *Mon. Weath. Rev.,* **118**, 2288–2311.

Sekelsky S. M., W. L. Ecklund, J. M. Firda, K. S. Gage and R. E. McIntosh, 1999: Particle size estimation in ice-phase clouds using multifrequency radar reflectivity measurements at 95, 33 and 2.8 GHz. *J. Appl. Meteor.,* **38**(1), 5–28.

Slingo, A., and J. M. Slingo, 1988: The response of a general circulation model to cloud long-wave radiative forcing. I: Introduction and initial experiments. *Quart. J. Roy. Meteor. Soc.,* **114**, 1027–1062.

Stubenrauch, C. J., A. D. DelGenio and W. B. Rossow, 1997: Implementation of subgrid cloud vertical structure inside a GCM and its effect on the radiation budget. *J. Climate,* **10**, 273–287.

Sun, Z., and K. P. Shine, 1995: Parameterization of ice cloud radiative properties and its application to the potential climatic importance of mixed-phase clouds. *J. Climate*, **8**, 1874–1888.

Sundqvist, H., 1993: Inclusion of ice phase of hydrometeors in cloud parameterization for mesoscale and largescale models. *Beitr. Phys. Atmos.,* **66**, 137–147.

Thomas, L., J. C. Cartwright and D. P. Wareing, 1990: Lidar observations of the horizontal orientation of ice crystals in cirrus clouds. *Tellus,* **42B**, 211–216.

Tian, L., and J. A. Curry, 1989: Cloud overlap statistics. *J. Geophys. Res.,* **94**, 9925–9935.

Tremblay, A., A. Glazer, W. Yu and R. Benoit, 1996: A mixed-phase cloud scheme based on a single prognostic equation. *Tellus A*, **48**, 483–500.

Wilson, D. R., and S. P. Ballard, 1999: A microphysically based precipitation scheme for the UK Meteorological Office Unified Model. *Quart. J. Roy. Meteor. Soc.,* **125**, 1607–1636.

Wylie, D., P. Pironen, W. Wolf and E. Eloranta, 1995: Understanding satellite cirrus cloud climatologies with calibrated lidar optical depths. *J. Atmos. Sci.,* **52**, 4327–4343.